5-2010

A Targeted Modeling Study of the Interaction Between a Supercell and a Preexisting Airmass Boundary

Jennifer M. Laflin
University of Nebraska at Lincoln, jenni.laflin@gmail.com

A TARGETED MODELING STUDY OF THE INTERACTION BETWEEN A SUPERCELL AND A PREEXISTING AIRMASS BOUNDARY

by

Jennifer M. Laflin

A THESIS

Presented to the Faculty of

The Graduate College at the University of Nebraska

In Partial Fulfillment of Requirements

For the Degree Master of Science

Major: Geosciences

Under the Supervision of Professor Adam L. Houston

Lincoln, Nebraska

May, 2010

A TARGETED MODELING STUDY OF THE INTERACTION BETWEEN A SUPERCELL AND A PREEXISTING AIRMASS BOUNDARY

Jennifer Meghan Laflin, M. S.

University of Nebraska, 2010

Adviser: Adam L. Houston

It is theorized that supercell thunderstorms account for the majority of significantly severe convective weather which occurs in the United States, and as a result, it is necessary that the mechanisms which tend to produce supercells are recognized and investigated. Airmass boundaries have been identified as a preferred location for supercell development due to the enhanced horizontal vorticity and forced ascent that are found along the boundary. This study examines the specific influence of a preexisting airmass boundary on supercell development through a set of idealized simulations. These simulations are based on a supercell which formed along an outflow boundary in the panhandle of Texas on 25 May 1999, and involve both homogeneous environments from the warm and cool sides of the boundary, as well as a representation of the actual environment with a boundary present. Detailed analyses of these simulations are then performed to determine the specific influence of the preexisting airmass boundary on supercell formation and morphology. It was found that the airmass boundary has three main impacts on the simulated storm: 1) enhancement of the updraft by forced ascent along the boundary, which allows a stronger right-splitting storm to develop, 2) production of a gust front through a combination of storm outflow and the cool

airmass, which allows the storm to transition away from precipitation and continually draw in warm air, and 3) provision of enhanced horizontal vorticity that supports the development and maintenance of a low-level mesocyclone.

Chapter 1

Introduction

A specific class of thunderstorms known as a supercell (Browning 1964) is defined by having a deep (approximately one third of the depth of the storm), persistent (lasting ~30 min or greater) mesocyclone (vertical vorticity ≥ 0.01 s^{-1}; Moller et al. 1994; Doswell 2001). Supercell thunderstorms have been correlated to a majority of the significantly severe weather associated with deep convection such as hail with diameter ≥ 5 cm, non-tornadic wind gusts ≥ 33 m s^{-1} and significant tornadoes (EF-3 and greater) and account for a large portion of damage which results from thunderstorms (Moller et al. 1994, Doswell 2001). Advanced warning of supercell thunderstorms is necessary to protect life and property and for this reason, it is important to recognize the mechanisms and environments that tend to produce supercell thunderstorms.

A number of studies have focused on environments that favor the development of supercell thunderstorms or, rather, the formation of a supercell from existing deep convection. For example, it has been found that moderate convective available potential energy (CAPE), high shear, and low convective inhibition (CIN) are often found where supercells develop (Rasmussen and Blanchard 1998; Thompson et al. 2003). Parameters have been developed that

combine shear and CAPE and can discriminate between convective modes, such as storm-relative helicity (SRH; Davies-Jones 1984), the energy-helicity index (Hart and Korotky 1991; Davies 1993), the bulk Richardson number (BRN; Weisman and Klemp 1982), the vorticity generation parameter (Rasmussen and Blanchard 1998), and the supercell composite parameter (SCP; Thompson et al. 2003), among others. Studies such as these, as well as the use of parameters in operational forecasting, have lead to the creation of thresholds or benchmark values to distinguish between convective modes, and by calculating the values of these parameters, an environment can be diagnosed as supportive or unsupportive of supercells. However, these values are inherently flawed in that the soundings from which they were calculated may not be representative of the storm's environment (Houston et al. 2008). In addition, it is also important to recognize mechanisms that create environments supportive of supercells. While optimal values of CAPE and environmental shear can be created by a favorable synoptic pattern, mesoscale features such as an airmass boundary can enhance an environment that is marginally supportive, or even unsupportive, of supercells on a larger scale. While the introduction of a mesoscale feature may create more favorable values for parameters such as shear, it also enhances the environment in methods that are not captured through parcel theory, such as locally enhanced vertical motion or additional environmental vorticity.

An airmass boundary is most simply defined as a demarcation between two airmasses with different densities, usually characterized by a temperature difference in the range of five to ten kelvins, and can be readily observed through

satellite, radar, and surface observations (Maddox et al. 1980). Preexisting airmass boundaries are those that are not formed by the storm in consideration, and thus exclude the storm's own gust front. Examples of a preexisting airmass boundary include an outflow boundary created by another storm or by convection that has dissipated or exited the area, or a synoptic front such as a cold or warm front.

Although a boundary comprises the area between two relatively homogeneous environments, the local boundary environment is quite different than either of the surrounding airmasses (Maddox et al. 1980). This local environment is quite complex, and has profound implications for convection. Several properties of an airmass boundary help to support both storm longevity and rotation in thunderstorms, thus enhancing an environment to become more supportive of supercells. As denser air wedges underneath the less dense air above, air parcels are forced upward (Figure 1.1), creating lift which strengthens the storm's updraft and assists with storm maintenance and longevity. In environments with low CAPE or a large area of CIN near the surface, the forced ascent along an airmass boundary could promote updraft maintenance in an environment that may otherwise be detrimental to the storm. An area of moisture convergence is also present along boundaries (Maddox et al. 1980), which lowers the lifted condensation level (LCL) and level of free convection (LFC) and can extend into the mid-levels, decreasing the chance for parcel dilution (Houston and Niyogi 2007). In addition to forced ascent and moisture convergence, boundaries also generate vertical vorticity via the four components of the vertical vorticity tendency equation:

$$\frac{\partial \zeta}{\partial t} = -(V \cdot \nabla \zeta) - (\delta \zeta) - \left(\frac{\partial w}{\partial x}\frac{\partial v}{\partial z} - \frac{\partial w}{\partial y}\frac{\partial u}{\partial z}\right) + \left(\frac{\partial D_v}{\partial x} - \frac{\partial D_u}{\partial y}\right) \quad (1.1)$$

which are, from left to right, advection of vertical vorticity, stretching of vertical vorticity, tilting of horizontal vorticity, and mixing. Horizontal vorticity is generated via the terms in the horizontal vorticity equations:

$$\frac{D\omega_x}{Dt} = \left[\frac{\partial u}{\partial z}\frac{\partial v}{\partial x} - \frac{\partial w}{\partial x}\frac{\partial u}{\partial y}\right] - \left[\left(\frac{\partial v}{\partial y} + \frac{\partial w}{\partial z}\right)\omega_x\right] + \left[c_p \frac{\partial \bar{\theta}}{\partial z}\frac{\partial \pi}{\partial y} + \frac{\partial B}{\partial y}\right] + \left[\frac{\partial D_w}{\partial y} - \frac{\partial D_v}{\partial z}\right] \quad (1.2a)$$

$$\frac{D\omega_y}{Dt} = \left[\frac{\partial w}{\partial y}\frac{\partial v}{\partial x} - \frac{\partial v}{\partial z}\frac{\partial u}{\partial y}\right] - \left[\left(\frac{\partial u}{\partial x} + \frac{\partial w}{\partial z}\right)\omega_y\right] + \left[c_p \frac{\partial \bar{\theta}}{\partial z}\frac{\partial \pi}{\partial x} + \frac{\partial B}{\partial x}\right] + \left[\frac{\partial D_u}{\partial z} - \frac{\partial D_w}{\partial x}\right] \quad (1.2b)$$

which are, from left to right, tilting, stretching, solenoidal, and mixing. The two primary ways that horizontal vorticity is generated along an airmass boundary are: 1) through a vertical pressure gradient at the head of the boundary via the solenoidal term, and 2) by enhanced vertical shear in the cooler airmass. This enhancement of vertical shear is created by backing winds in the cooler airmass, due to the environment's attempt to reach thermal wind balance (Maddox et al. 1980). Environments with low vertical shear – and thus low ambient horizontal vorticity – can be enhanced by additional horizontal vorticity along an airmass boundary, creating the potential for the development of a mesocyclone. Increased positive vertical vorticity along the boundary, whether generated through stretching of preexisting vertical vorticity along the boundary or tilting and stretching of horizontal vorticity found in the denser side of the boundary, can directly supplement the mesocyclone as it interacts with a boundary environment.

The connection between supercell development and airmass boundaries has been documented in a number of previous studies (Maddox et al. 1980, Markowski et al. 1998, Atkins et al. 1999, etc.). Atkins et al. (1999) found that a low-level mesocyclone is longer-lived and stronger when the storm encounters an airmass boundary. In addition, they hypothesized that the mechanism for low-level mesocyclogenesis is fundamentally different in the presence of an airmass boundary. By observing a number of cases in which supercell thunderstorms formed in non-supercellular environments, Maddox et al. (1980) suggest that both a local increase in moisture convergence along the boundary and changes to relative vertical vorticity in the boundary layer support the intensification of thunderstorms over boundaries. Markowski et al. (1998), in an overview of tornado-producing supercells associated with boundaries during VORTEX-95, suggest that the horizontal vorticity enhancement such as that created by an airmass boundary is necessary for low-level mesocyclogenesis, with the exception of extremely favorable conditions, such as an outbreak day. From these studies, it is apparent that airmass boundaries can be important for supercell development, both in supercellular and non-supercellular environments.

The work of Atkins et al. (1999) and Fierro et al. (2006) took similar approaches to investigating the role of airmass boundaries in supercell development. Fierro et al. (2006) were primarily concerned with updraft strength and the response of electrification in the simulated storm; however, Atkins et al. (1999) were motivated by questions very similar to those posed by the current study. Therefore, their study requires further review. Atkins et al. (1999) made use

of numerical modeling to simulate deep convection along a preexisting airmass boundary in a supercell environment, and examined the impact of the boundary on the low-level mesocyclone by making comparisons with an additional simulation in a homogeneous representation of the warm side of the boundary. Their study concluded that a significant portion of the air which travels into the low-level mesocyclone originates in the cool side of the boundary; however the role of the cooler airmass in the development of the mid-level mesocyclone is not discussed. In addition, the cool side airmass is not considered for a control experiment. Finally, the boundary in the simulation is considered a static entity and trajectories are only calculated at one time, therefore it is not possible to address how the boundary and surrounding airmasses are contributing as the mesocyclone develops. The current study seeks additional insight on the role of the cooler airmass by using the cool airmass as a control experiment, and also seeks to analyze how the role of the airmass boundary changes throughout the storm's life cycle. The results of this study will be compared to those of Atkins et al. (1999) to determine if similar results are produced, and to determine whether or not these results can be applied to mid-level rotation.

Although previous studies address the role of airmass boundaries in mesocyclogenesis, the individual contributions of additional horizontal vorticity or enhanced vertical velocity have not been attributed to supercell development. A theoretical argument can be made for how airmass boundaries could support supercell development; however these processes have not been observed separately. Strictly observational studies do not allow for a comparison to a control

experiment, therefore it is impossible to know how storms would develop without a boundary present. Mesoscale numerical modeling, however, allows for a control simulation, as well as high spatial and temporal resolution of multiple variables and a much more detailed diagnosis of the boundary and surrounding environment.

Through the use of numerical modeling on the mesoscale, this study will investigate the specific properties of an airmass boundary that are supporting supercell development and will examine the individual contributions of these properties. To do this, convection will be simulated in three environments: one with an airmass boundary present, and two horizontally homogeneous environments that represent the warm (less dense) and cool (denser) sides of the airmass boundary. The boundary simulation will allow for analysis of both the boundary and the progression and development of the simulated storm as it interacts with the boundary, while the homogeneous simulations will allow for comparison of mesocyclone strength and longevity between the storms produced in the boundary versus homogeneous environments. These simulations will be loosely based on an actual event in which a supercell formed along an airmass boundary.

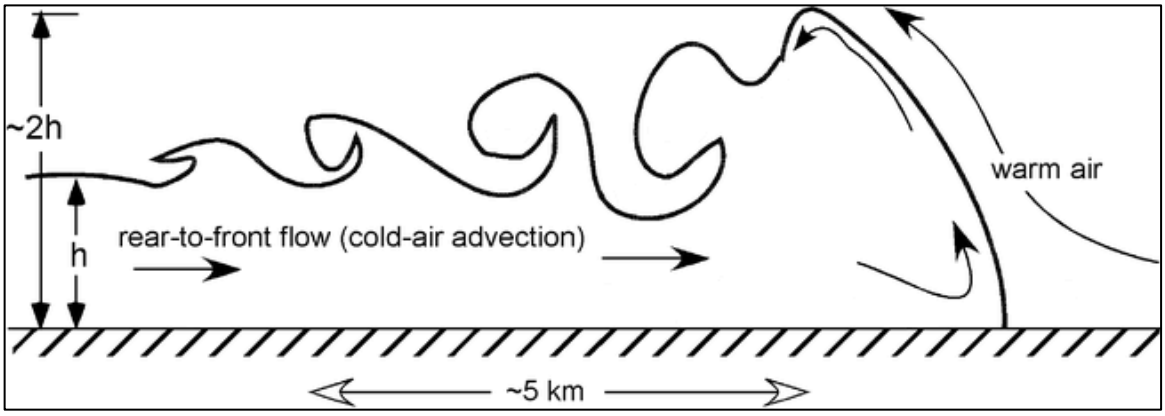

Figure 1.1. A conceptual model of an airmass boundary cross section, adapted from Geerts et al. 2006.

Chapter 2

Methodology

To study the effect of a preexisting airmass boundary on supercell formation, deep, moist convection is simulated in three environments: one representing the warm (less dense) side of a boundary, one representing the cool (denser) side of a boundary, and one with a boundary present. An idealized model is used to simulate deep convection for this study, in order to isolate the role of the preexisting airmass boundary on the development of the mesocyclone. The idealized modeling platform limits other factors that may have a role in modifying the storm's convective mode, such as radiation, evapotranspiration, or surface friction, while also allowing for a thorough and detailed analysis of the airmass boundary and simulated storms.

The model used in this study is the Illinois Collaborative Multiscale Model for Atmospheric Simulations (ICOMMAS; Houston 2004), a non-hydrostatic, finite difference model. ICOMMAS is similar to its predecessor, COMMAS (Wicker and Wilhelmson 1995), but was designed specifically to study the relationship between convective initiation and airmass boundaries. A full description of ICOMMAS is available in Houston (2004). In the horizontal plane, open lateral boundary conditions are selected, which treats any distance outside the domain as a reflection of the simulated domain (Klemp and Wilhelmson 1978). The microphysics scheme

used is a single moment, three-phase ice parameterization (Gilmore et al. 2004). Simulations are completely idealized and so do not include a land surface model, surface layer scheme, or an atmospheric radiation scheme.

For model initialization, the case chosen is an HP supercell that formed in the panhandle of Texas on 25 May 1999. An outflow boundary, created by convection which exited the area well before storm initiation, is apparent both in satellite data (Figure 2.1) and North American Regional Reanalysis data (NARR; Mesinger et al. 2006; Figure 2.2), and was also documented in a previous study (Dostalek et al. 2004). The storm considered in this study formed approximately 5 km to the west of the airmass boundary just after 20 UTC and drifted slowly to the northeast through 22 UTC. As the cell crossed the boundary, it acquired rotation and could be defined as supercellular. The mesocyclonic rotation of the storm caused it to deviate from its previous storm motion and begin tracking to the east southeast. This storm remained supercellular in the cool side of the boundary through 0022 UTC on 26 May (Figure 2.3).

The warm side sounding and wind profile used for model initialization (Figures 2.4 and 2.5) is interpolated from the NARR at a point approximately 30 km away from the boundary in the warm side. The time used for the proximity sounding is 21 UTC, which falls within an hour of the time convection initiates along the outflow boundary. Rawinsondes were launched on 25 May 1999 at 12 UTC and 18 UTC by the National Weather Service in Amarillo, TX and at 12 UTC in Midland, TX, but neither sounding is located in the warm side environment; thus, model data are required to accurately represent the appropriate environment. To identify the

outflow boundary characteristics such as the temperature, moisture, and wind profiles, as well as the depth of the boundary, another proximity sounding is taken at a point 30 km into the cool side, and is compared to the warm side proximity sounding.

For initialization of the homogeneous simulation representing the cool side of the boundary, a sounding is taken from the boundary simulation, approximately 30 km into the cool side. Although the density current is prescribed to best represent the boundary observed both in the NARR and surface observations, the simulated cool side environment and the cool side proximity sounding from the NARR are not identical. In order to maintain consistency with the environment in the boundary simulation, it is necessary to use a sounding from the cool side of the boundary simulation (Figures 2.4 and 2.5) for initialization of the cool side. The warm and cool side simulations are horizontally homogeneous at model initialization, while the simulation which represented the boundary environment is initialized by the warm side sounding, with the addition of an outflow boundary covering the northern half of the domain. The initial vertical wind profile used for initialization of the boundary simulation is backed 45 degrees from the original warm side environment, so that the convergence observed along the northwest-southeast oriented boundary in the case study is similar to that along the simulated east-west boundary.

As an initial prediction of whether to expect supercells or non-supercells in the homogeneous simulations, CAPE, environmental shear, the SCP, and the BRN are computed from both the warm side and cool side soundings and compared to

expected values for supercell environments, such as those found by Rasmussen and Blanchard (1998) and Thompson et al. (2003); a summary of these values, as well as typical values for a supercell environment (Thompson et al. 2003) can be found in Table 2.1. On the warm side of the boundary, the CAPE and CIN are well within the expected range for supercells; however the environmental shear is relatively weak, which results in marginal values for 0-6 km shear and non-supercellular values for 0-3 km SRH and the SCP. In addition, the sounding is very dry, and an environment low in moisture can potentially lead to dilution and a decrease in the overall instability of the parcel (Ziegler and Rasmussen 1998, Houston and Niyogi 2007). Values in the cool side are closer to what would be expected in a supercell environment, with supercellular values of 0-6 km shear, the SCP, and CAPE, and a marginal value of 0-3 km SRH. However, the high value of CIN would seem to make it nearly impossible for convection to develop without some external forcing.

Due to the argument that dilution could decrease the overall CAPE of the warm side storm, an additional warm side simulation is run with increased moisture throughout the depth of the sounding (Figure 2.6). To alter the moisture profile, the mixing ratio is given a constant slope of -5 g kg^{-1} per km from 1.2 km through 4 km, then is held at a constant relative humidity of 25 percent between 4 km and the top of the domain. Below 1.2 km, the mixing ratio in the modified warm side simulation is the same as the mixing ratio in the original warm side simulation. Once these modifications are made, the modified warm side simulation is initialized in the same manner as the original homogeneous simulation, but is not used to initialize a boundary simulation.

In the cool side simulation, the stable layer created by the airmass boundary has the potential to inhibit convection, since it creates a large value of CIN for parcels originating from the surface. To mitigate this, an additional simulation in the cool side is run in which the vertical position of the thermal bubble used to initiate convection was based above the stable layer; in this case, at 750 m AGL. This resulted in the bubble being centered vertically at 1.5 km AGL, with the same radius and temperature/moisture perturbations as all other simulations. The same sounding used to initialize the original homogeneous cool side simulation is also used for initialization of the modified cool side simulation.

In order to capture the supercellular nature of a convective thunderstorm while limiting simulations to reasonable computational time and resources, a grid spacing of 500 m is used in the horizontal, with a vertical grid spacing stretching from 100 m in the boundary layer to 500 m in the upper troposphere. This grid spacing resembles those used in other studies which consider phenomena on a similar scale (Houston 2004). The full model domain is 80 km in both horizontal directions by 19.5 km in the vertical. Soundings that are used to initialize the model have a maximum height of approximately 19.8 km, which limits the size of the domain in the vertical; in addition, the grid is translated at each time step to follow the storm, which allows for a relatively small horizontal domain.

For all simulations, a thermal bubble is used to initiate convection. The bubble has a horizontal radius of 10 km and a vertical radius of 750 m, and is centered at 750 m AGL. A 3 K perturbation is present in the center of the bubble and decreases to zero on the edges. The simulation containing a boundary is initialized

with a slab-symmetric density current which has temperature and water vapor mixing ratio perturbations that are prescribed to best resemble the boundary observed in the selected case study. The same thermal bubble which initiates convection in homogeneous simulations is used to initiate convection in the boundary simulation instead of allowing convective initiation along the boundary itself. This is done to represent a preferential location for convective initiation along the outflow boundary and to prevent convection from forming in a line throughout the length of the domain. Due to the environmental wind profile, the boundary and bubble have different propagation speeds; therefore in the boundary simulation, the bubble is positioned in the warm side of the domain so that the storm will begin producing precipitation as it enters the boundary environment.

To create the airmass boundary, an 1100 m deep block of cold air is initialized in the warm side environment, and covers the northern half of the domain. Initially, the temperature perturbation inside the density current is a constant -4 K, and the water vapor mixing ratio perturbation decreases from 2.1 g kg^{-1} at the surface to 1.0 g kg^{-1} at the top. This initial block of cold air is unrepresentative of an actual boundary, since the temperature and moisture profiles have no gradient or variation in the horizontal or vertical directions. To mitigate this effect, the environment is first initialized in a shallow domain which is 1500 m deep. The lifted condensation level of the warm side base state is 1595 m AGL, so the shallow domain allows the environment to adjust without initiating convection. After 3600 s, the shallow domain (Figure 2.7) is seeded into the full three-dimensional domain, as in Houston and Niyogi (2007). At this point in the

initialization procedure, deep moist convection could develop, but precipitating convection does not form. Instead of the boundary itself initiating convection, the previously described thermal bubble is used to initiate the actual storm.

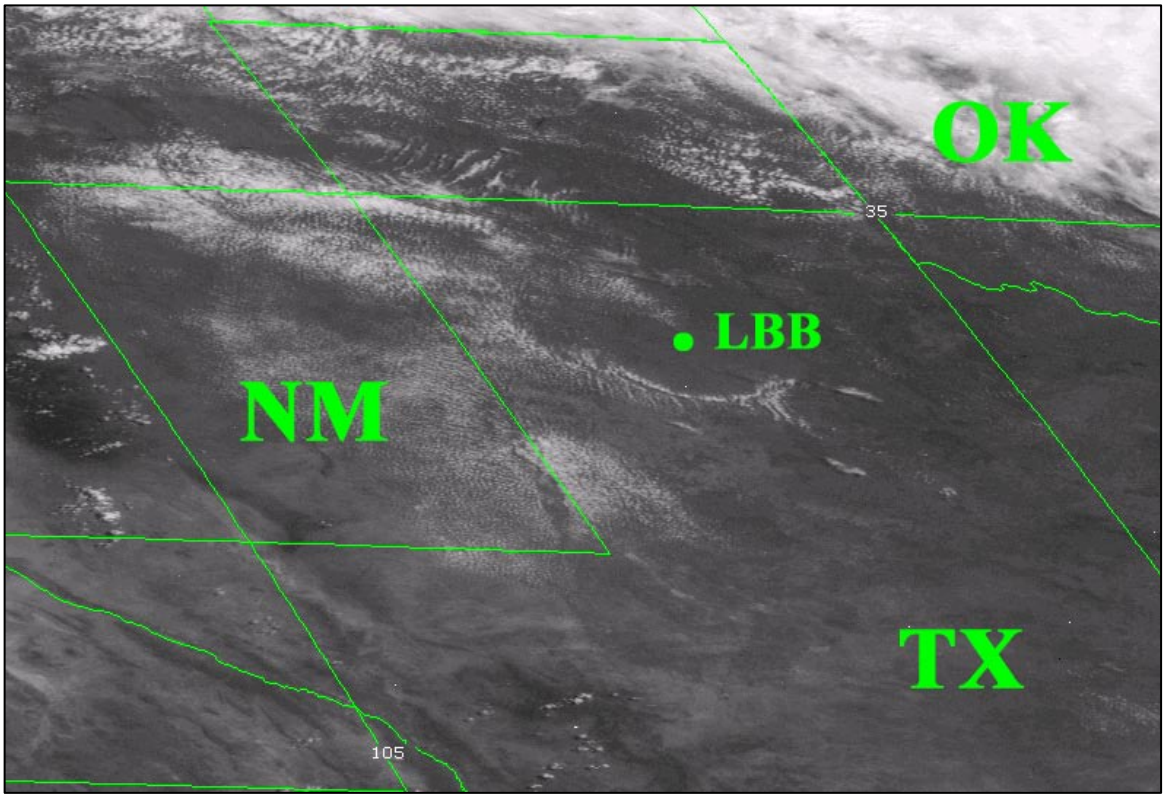

Figure 2.1. A GOES-10 satellite image of the outflow boundary observed in the panhandle of Texas at 1715 UTC on 25 May 1999.

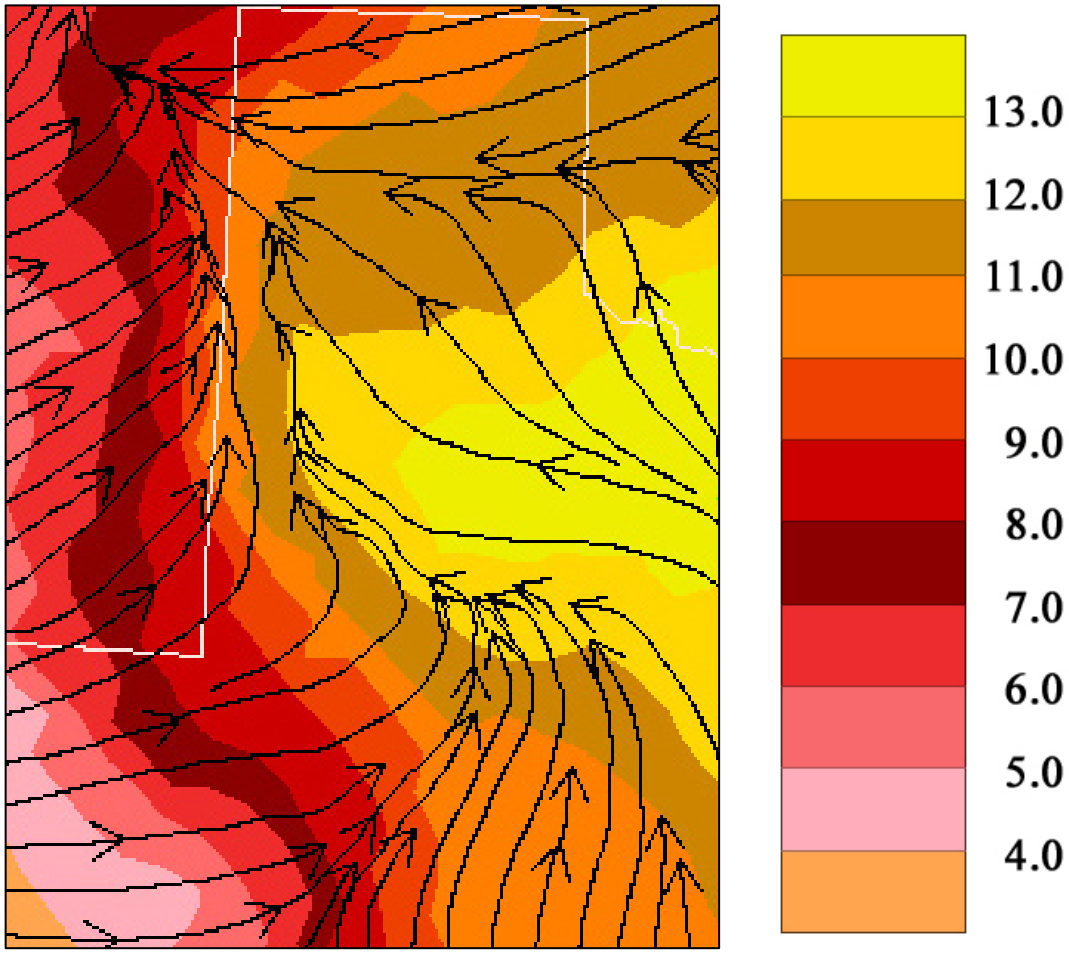

Figure 2.2. The case study outflow boundary resolved in NARR data at 21 UTC. Shading is mixing ratio at 2 m AGL, contoured at a 1 g kg^{-1} intervals, following the legend on the right. 10 m streamlines are plotted in black.

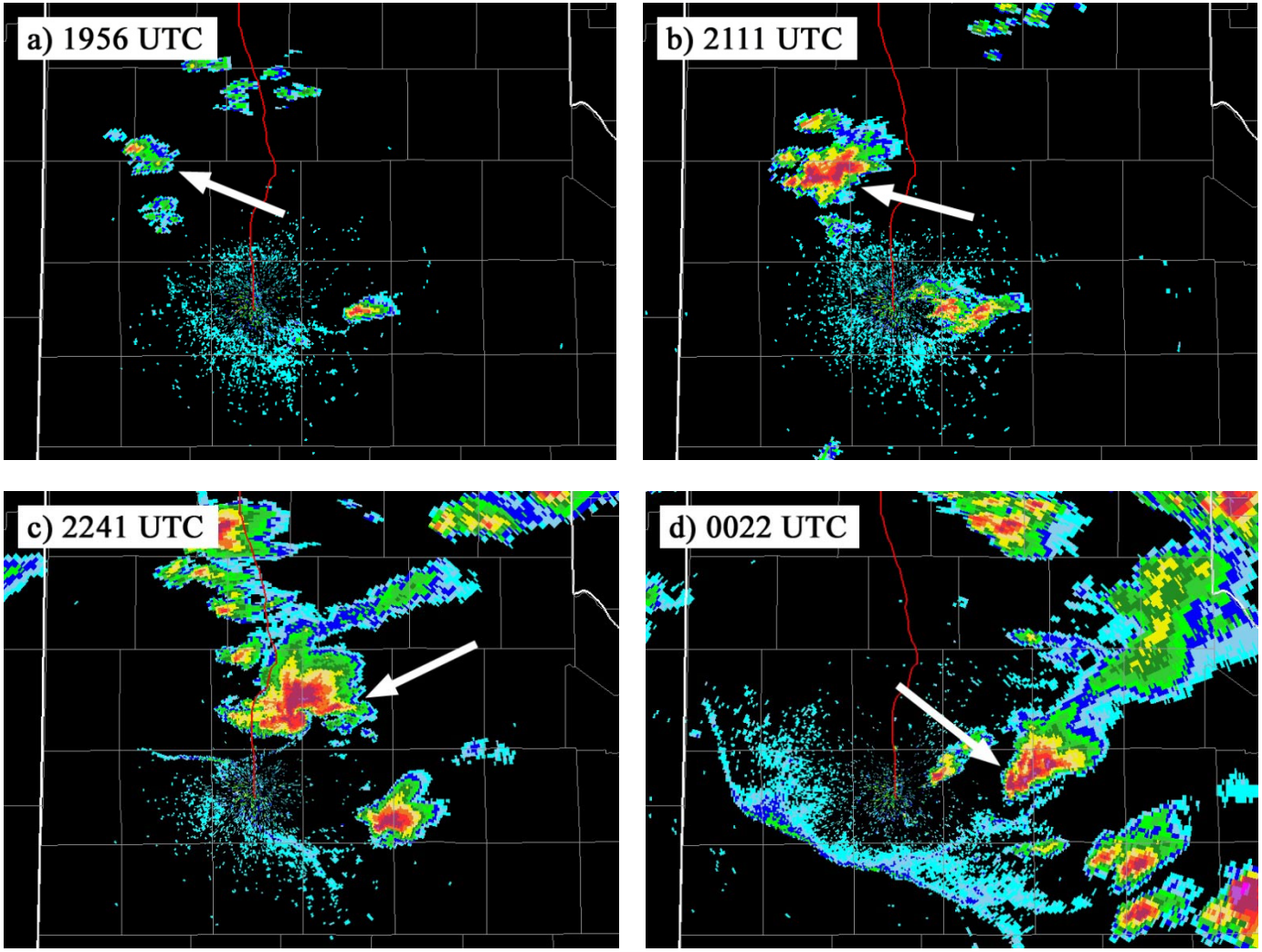

Figures 2.3. Reflectivity of the case study storm at (a) 1956 UTC, (b) 2211 UTC, and (c) 2241 UTC on 25 May 1999, and (d) 0022 UTC on 26 May 1999. The case study storm is denoted in each panel by a white arrow.

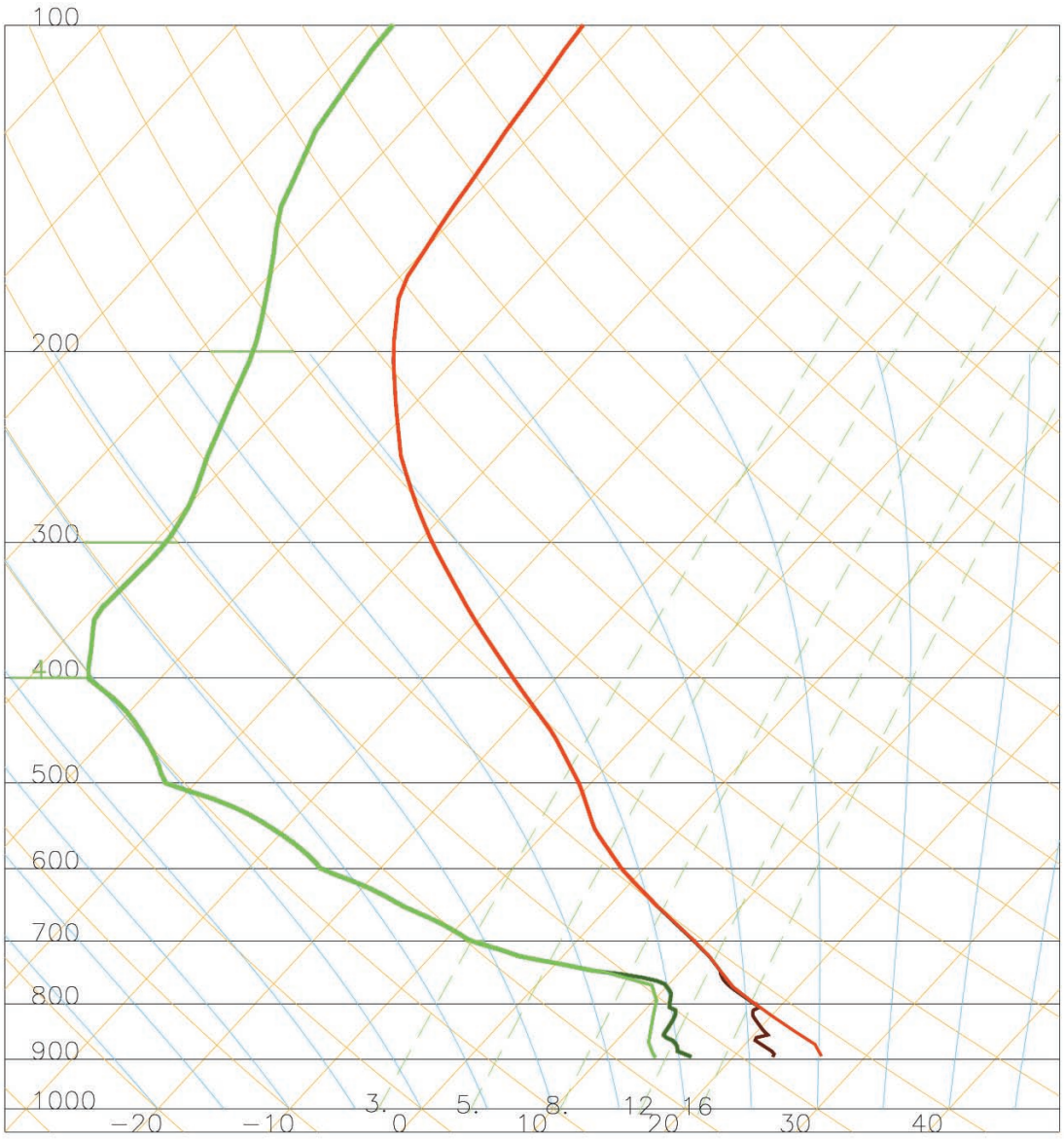

Figure 2.4. The warm side sounding (light green and red) and cool side sounding (dark green and dark red) used to initialize the homogeneous simulations.

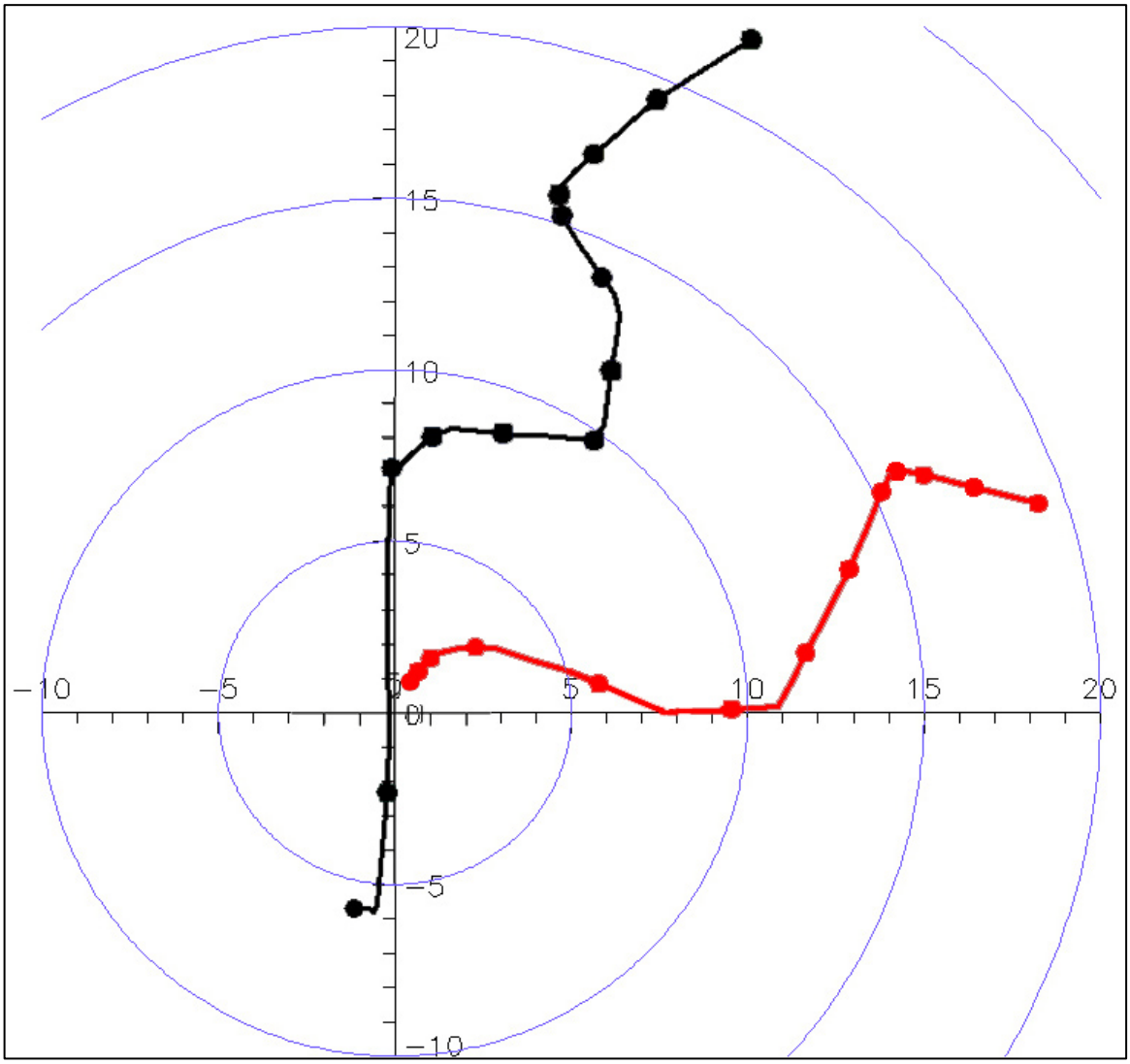

Figure 2.5. The warm side hodograph (red) and cool side hodograph (black) used to initialize the homogeneous simulations.

Table 2.1. A summary of selected severe weather forecasting parameters in the warm and cool side environments, and a comparison to threshold values for a supercell environment (Thompson et al. 2003).

	Warm	**Cool**	**Supercell**
SBCAPE (J kg^{-1})	2390	2186	≥ 800
CIN (J kg^{-1})	28	110	≤ 50
0-6 km shear (m s^{-1})	18.0	26.7	≥ 20
0-3 km helicity (m^2 s^{-2})	53	160	≥ 100
SCP	1.15	9.76	≥ 2.0

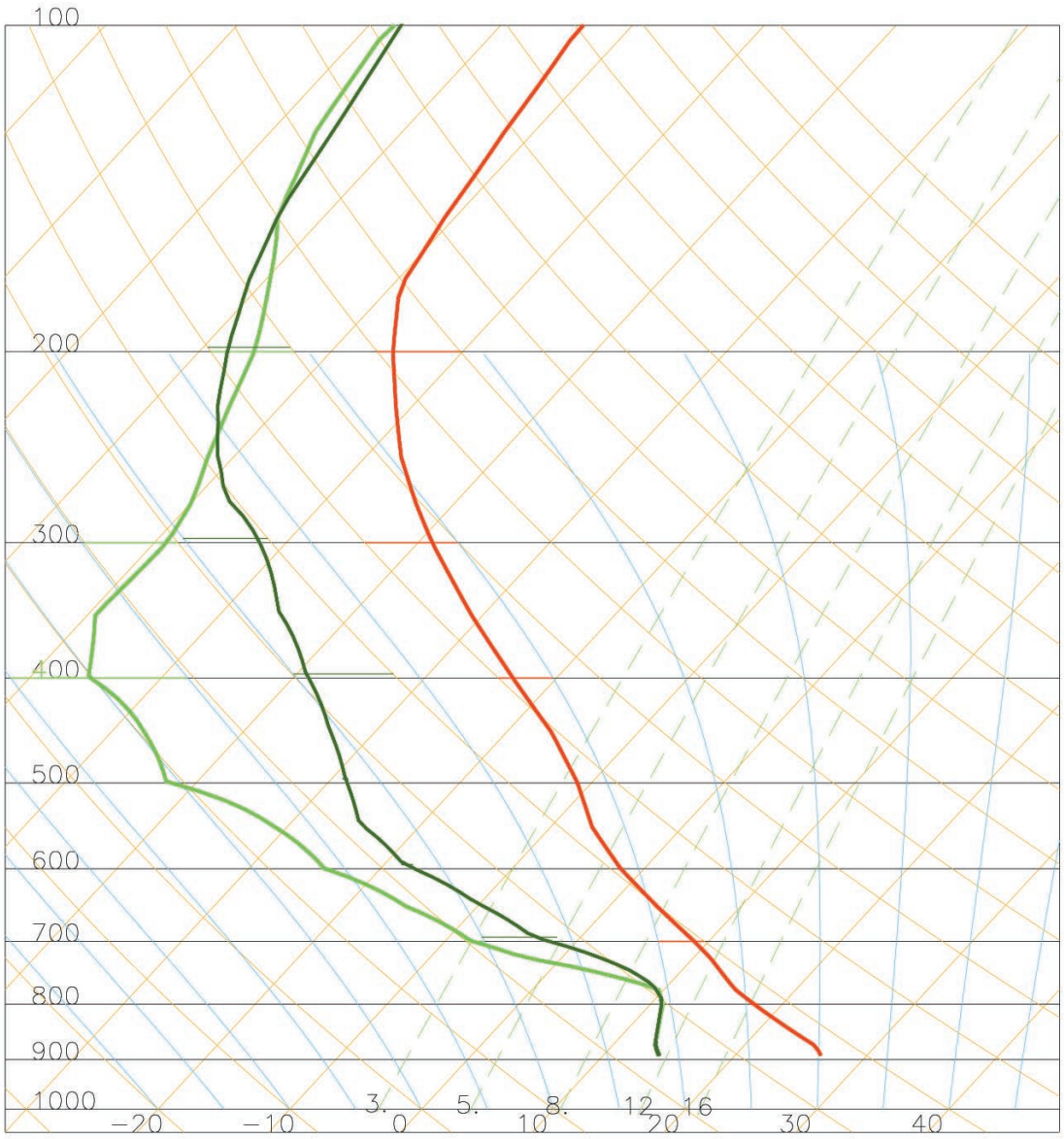

Figure 2.6. A comparison of the moisture profile in the original warm side sounding (light green) and modified warm side sounding (dark green) used to initialize the homogeneous simulations.

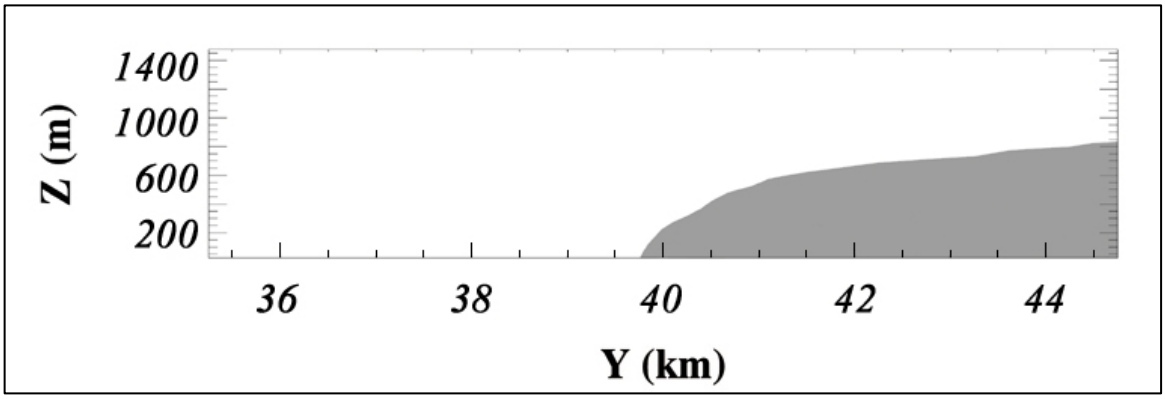

Figure 2.7. The simulated outflow boundary in the channel domain before being seeded into the full domain at 3600 s. Shading is potential temperature perturbation < 0 K.

Chapter 3

Results

The results of the simulations are presented in this chapter in four sections: time series analysis, a high-precipitation supercell (HP) analysis, storm split analysis, and trajectory analysis. Time series analyses will overview the timing and progression of precipitation at the surface, vertical vorticity, and updraft strength, in order to create associative relationships and draw preliminary connections between the environments and simulated storms. As a method of comparing simulated storms, the HP analysis aims to quantify the HP character of the model output. This is done using a proxy for reflectivity in the model results, as well as a method which is loosely based on that described in Beatty et al. (2004; hereafter, B04). The method proposed by B04 uses the position of a supercell's reflectivity centroid relative to the updraft to determine whether or not a supercell is HP, based on whether the centroid is behind or ahead of the updraft with respect to storm motion. While this method captures a widely accepted view that heavier precipitation behind a supercell's updraft would cause that storm to be defined as HP, it does not encompass the most fundamental characteristic of the HP morphology. Based on the definition that precipitation falling in the mesocyclone of a supercell makes it HP

(Moller et al. 1994), it is more logical to quantify HP character via the amount of precipitation present in the mesocyclone.

To calculate this quantity, an HP algorithm is created to calculate a dimensionless HP value from model output. The location of the mesocyclone is defined as the location of the maximum value of vertical vorticity, while the diameter of the mesocyclone is determined by the width of vertical vorticity exceeding 0.01 s^{-1}. The diameter and center point of the mesocyclone are computed between 1.5 and 6 km AGL in order to avoid noise in the data created by the airmass boundary, and the maximum diameter through these levels is used as the final mesocyclone diameter. To best represent how precipitation is affecting the low-level mesocyclone, the center point of the mesocyclone located at cloud-base height is used for the mesocyclone location. Once the location and diameter are calculated, the HP algorithm searches through the simulated reflectivity in each grid box within the mesocyclone diameter and checks to see whether the value is greater than or equal to a "convective precipitation" threshold; in this case, 40 dBZ. The number of grid boxes with reflectivity exceeding the threshold value is then divided by the total number of grid boxes in the mesocyclone. This percentage can be calculated at each time step and compared between simulations, allowing an evaluation of whether a simulated storm is more or less HP than another.

While B04's method of determining supercell morphology gives a yes or no answer to whether a storm is HP at any given time, the method described above can be used to determine a storm's HP character or, rather, to what degree the storm could be defined as HP. While there is no benchmark value defining if a storm is HP

or non-HP, this algorithm allows for an evaluation of the progression of HP character with time, as well as comparisons between different simulations. For the purpose of this study, the algorithm is used to compute an HP value for each time step in which a low-level mesocyclone is present, so that HP values can be compared between simulations and between times in a single simulation. HP values are used as a more detailed method of comparing the progression of the low-level mesocyclones produced in each simulation and their relationship to surface precipitation. Another time series is computed from the HP analysis, which captures the longevity of the simulated storm and the storm's response as precipitation impacts the low-level mesocyclone.

Early in the boundary simulation, the right moving storm undergoes a major transition after a split. The processes that lead to the split and the impacts of the split on the simulated storm are described in detail in the storm splitting analysis section. As a final method of analyzing the results, trajectories are computed in the boundary simulation to determine the source regions of vertical vorticity in the mesocyclone, and serve as a detailed method of examining the impact of the boundary on the simulated storm's progression and overall strength throughout its life cycle. In this study, trajectories are initialized in a vertical slice within an area of interest, such as the mid-level mesocyclone or low-level updraft, and are then backwards integrated in time to determine the position of each tracer at preceding times. Plan view images of trajectory paths make use of different colors to signify height of the trajectory through time, which allows for a comparison of the trajectory's track to a vertical slice at a specified time. In addition to plan views of

the trajectory paths, a number of variables can be calculated for each trajectory at any given time. From these calculations, time series and vertical profiles of specific variables can be plotted and analyzed for trajectories.

3.1 Time Series Analysis

For the purpose of comparison in the time series analysis, a storm is considered to have mesocyclonic rotation when the vertical vorticity in that storm reaches or exceeds a value of 0.01 s^{-1}. The storm is still not considered a supercell until reaching the time constraint (mesocyclonic rotation for greater than ~30 minutes; Moller et al. 1994, Doswell 2001) in addition to the vorticity threshold; however for the sake of comparison between simulations, vertical vorticity is measured at each time step and used as a means of evaluating each storm, regardless of whether or not it reaches supercell criteria. Visualization of radar reflectivity is a familiar method of recognizing storm structure and morphology; therefore a proxy for radar reflectivity is calculated from model data and used to analyze and compare model simulation results (Smith et al. 1975). This proxy creates values that are comparable to reflectivity values from the Weather Surveillance Radar 88-Doppler, and is calculated from the surface precipitation rates of rain and hail. Plots of simulated reflectivity are used within the time series analysis, in order to provide an overview of the simulated storm's structure and progression throughout its life cycle.

The warm side simulation is run for 7200 s (2 hours), with the thermal bubble released at 0 s. Convection is considered to initiate when cloud ice is first present in the domain, in this case at 610 s, or just over ten minutes into the simulation. Precipitation forms at the surface around 1980 s and dissipates at

4320 s, or 39 minutes after precipitation reaches the surface. The approximate storm motion is ENE at 9.5 m s^{-1}, although the motion is somewhat erratic throughout the simulation. Although the storm obtains mesocyclonic rotation before precipitation reaches the surface, the mesocyclone in the simulated storm is considered to be present only when precipitation is present at the surface; therefore, from 1980 s. Mesocyclonic rotation persists in the mid-levels until 3780 s, which gives the mesocyclone a lifetime of approximately 30 minutes (Table 3.1). Maximum vertical vorticity found in this storm is on the order of 0.03 s^{-1} and is present in the first 10 minutes of the mesocyclone's lifetime (Figure 3.1). The low-level mesocyclone – which is defined as mesocyclonic rotation present at cloud base (~1.5 km) – is obtained at 1980 s and lost at 2340 s, giving it a lifetime of only six minutes. The main updraft increases to 35 m s^{-1} before precipitation forms, reaches a secondary maximum of 20 m s^{-1} at 2700 s as the storm pulses upward in intensity, and then generally decreases in strength throughout the remainder of the simulation (Figure 3.2). A proxy for radar reflectivity of the simulated warm side storm is shown in Figure 3.3, which features multiple areas of mid-level rotation and the quick immersion of these mesocyclones into precipitation. Due to the presence of mesocyclonic rotation at mid-levels for 30 minutes, the warm side simulation can be defined as a supercell, albeit relatively short-lived.

To judge the impact of adjusting the warm side moisture profile, the modified warm side and original warm side simulations are compared. Although the overall simulated reflectivity and storm structure appear similar, the modified warm side storm is disorganized and possesses several short-lived areas of mesocyclonic

rotation, none of which persist 30 minutes or more (the longest-lived is presented in Table 3.1), and all of which quickly become imbedded in precipitation (Figure 3.4), similar to the warm side simulation. Convection initiates around 600 s, precipitation reaches the surface at 1920 s and is present through the end of the simulation. Vertical vorticity values in these short-lived spin-ups are on the order of 0.03 s^{-1} before dissipating again, which gives a wave-like pattern to the maximum vertical vorticity values throughout the domain as one circulation weakens and another strengthens (Figure 3.1). Vertical velocity displays a similar, but muted, wave-like pattern as the first updraft reaches a maximum of 32 m s^{-1} at 2640 s and a second updraft reaches 30 m s^{-1} at 3360 s (Figure 3.2). After all updrafts pulse upward, the vertical velocity and vertical vorticity values decline throughout the rest of the simulation.

The cool side simulation is also run for 7200 s, with the thermal bubble released at 0 s. Convection in this simulation initiates at 570 s, or just over nine minutes into the simulation, and precipitation reaches the surface at approximately 2130 s (~35 min). The simulated storm has cyclonic mid-level mesocyclones on both the right and left flanks of the storm when precipitation begins reaching the surface (Figure 3.5), and the right flank of the storm contains mesocyclonic rotation down to cloud base (~1 km). Low-level rotation dissipates on the right flank six minutes after precipitation formed, or at 2490 s. As the storm begins splitting into right and left moving components, the mesocyclonic rotation on the right flank begins dissipating altogether and falls below a vertical vorticity value of 0.01 s^{-1} at 2850 s (Figure 3.5c), the approximate time the two components separate.

Mesocyclonic rotation on the left flank of the left moving storm never reaches low levels, but persists until 5010 s. This gives the left flank mesocyclone a lifetime of 48 minutes and the right flank rotation a lifetime of twelve minutes (Table 3.1). Precipitation in the left mover dissipates at 5910 s, or 63 minutes after reaching the surface. Maximum vertical vorticity in the left flank mesocyclone is on the order of 0.03 s^{-1}, which occurs early in the simulation and decreases thereafter. Approximate storm motion of the left mover is 7.6 m s^{-1} to the NNW and the storm motion of the dissipating, right moving storm is approximately 9.4 m s^{-1} to the NE. Vertical velocity follows a similar trend; reaching a maximum of 36.5 m s^{-1} before precipitation reaches the surface, and decreasing overall after this point (Figure 3.2). This simulation provides a slightly longer-lived supercell in the left moving storm, despite the fact that a low-level mesocyclone never developed.

The modified cool side storm is very similar in overall structure and life cycle to the original cool side simulation; however, the left splitting storm is stronger and more persistent (Figure 3.6) in the modified case. Precipitation reaches the surface at 2130 s, and mesocyclonic rotation is present at the mid-levels on both flanks at that time (Figure 3.6a). At first, low-level rotation is not present on either flank; however mesocyclonic rotation develops at cloud base (~1 km) on the left flank at 2670 s. The low-level rotation is lost at 3570 s, and splitting occurs three minutes later at 3750 s, or around the time of the right flank rotation's demise. Mesocyclonic rotation persists at mid-levels in the left splitting storm until 6810 s, and precipitation at the surface is present through the end of the simulation. In this modified cool side simulation, the left split has a mesocyclone which persists for 78

minutes, while the rotation in the right splitting storm lasts 27 minutes (Table 3.1). Vertical vorticity values are similar to the original cool side simulation, with a maximum value of around 0.03 s^{-1} early in the simulation, and an overall decrease throughout the remainder of the simulation (Figure 3.1). Although the updraft in the modified cool side simulation is stronger than the original cool side simulation when precipitation forms, and peaks at a value of 53 m s^{-1} before precipitation forms, the same overall decreasing trend can be seen through the remainder of the simulation (Figure 3.2). Approximate storm motion of the left mover is 9.5 m s^{-1} to the NNW and the storm motion of the right moving storm is 7.3 m s^{-1} to the NE.

The storm produced in the boundary simulation is the final storm to be described. After the boundary stabilizes in the channel domain and is seeded into the full domain (3600 s), a thermal bubble is released. All times described in this section, as well as the times used on all time series and images, refer to elapsed time from the bubble release, such that the time the channel domain is seeded into the full domain and the bubble is released becomes 0 s. The initial grid motion is set to 7.5 m s^{-1} to the NE, and the bubble is placed so that the simulated storm encounters the boundary just as precipitation reaches the surface. Convection initiates at 570 s, and precipitation reaches the surface at 1920 s (32 min). Mesocyclonic rotation is present at the time precipitation forms at the surface (Figure 3.1) and is present throughout the end of the simulation, which was terminated at 14400 s, or just less than 4 hours after precipitation reached the surface (Table 3.1). The storm splits into left and right moving components at approximately 2640 s, and both contain mid-level mesocyclones; however the right mover is clearly dominant and contains

a low-level mesocyclone from 7200 s through the end of the simulation (Figure 3.7). The left moving storm propagates out of the domain around 8400 s, which is allowed so that the dominant right-moving storm can remain near the center of the domain. Vertical vorticity values on the order of 0.03 s^{-1} are associated with the left-moving storm, while maximum values of vertical vorticity on the order of 0.06 s^{-1} are associated with the right-moving storm (Figure 3.1). Unlike previous simulations, both vertical vorticity and vertical velocity show an increasing and then level trend of high values throughout the simulation. Vertical velocity generally increases through the first 7320 s, with some variation as the storm organizes, then remains around 50 m s^{-1} throughout the remainder of the simulation (Figure 3.2). Approximate storm motion of the right moving storm switches from 9.2 m s^{-1} to the NNE to 11.0 m s^{-1} to the ENE, while the storm motion of the left-moving storm is 8.3 m s^{-1} to the NNW. In this simulation, both the left and right moving storms contain a mesocyclone, and the right-moving storm is clearly a long-lived, persistent supercell.

The development of the updraft at early stages is complicated by the presence of the boundary. When compared to the homogeneous warm side, the updraft in the boundary simulation begins to increase beyond values seen in the homogeneous simulation as early as 1260 s (Figure 3.8); however, the updraft is not superimposed on the boundary until 2280 s (denoted in Figure 3.9). Although the main updraft does not encounter the forced ascent of the boundary directly until 2280 s, other effects of the boundary such as enhanced inflow help to support the updraft well before, which accounts for the differences between the homogeneous

and boundary simulations. The boundary environment is loosely defined as the area from 10 km into the warm side to 30 km into the cool side of the boundary (Markowski et al. 1998), so it is not surprising that the boundary storm would experience some enhancement before directly encountering the forced ascent. By 1260 s, the leading edge of the thermal bubble was centered approximately 5 km south of the boundary, or within the boundary environment.

Vertical velocity begins to level off before increasing again as the low-level updraft encounters the forced ascent (Figures 3.8 and 3.9). As the storm continues to propagate to the northeast, the updraft becomes tilted at low to mid levels. The low-level updraft is still strongest along the area of forced ascent, but the midlevel updraft continues to shift northeastward, and eventually separates from the updraft at low levels at approximately 2400 s. Meanwhile, the low-level updraft, augmented by the forced ascent of the boundary, begins increasing aloft, becoming evident at 5 km around 2760 s. This secondary updraft quickly becomes dominant, and the northern updraft dissipates completely by 3480 s. While this transition appears as a decrease in the overall maximum vertical velocity from 2520-2880 s (Figure 3.9), it is actually the transition between dominant updrafts. Beyond this point, an overall increasing trend is seen in vertical velocity throughout the simulation (Figure 3.2). Whether or not this is an indirect effect of the original direct augmentation of the vertical velocity, or merely that the second updraft developed in a more favorable location relative to the precipitation, is beyond the scope of this study. However, the trend in vertical velocity at low levels implies that the initial increase in updraft strength and development of the second updraft are direct results of the boundary;

after the storm propagates away from the boundary, a slight decrease is seen in the low-level vertical velocity, implying that forced ascent is no longer directly impacting the updraft. As the storm moves over the cooler airmass, direct augmentation of the vertical velocity from forced ascent is no longer plausible, thus effects other than forced ascent from the airmass boundary mostly likely dominate any increases seen in updraft strength.

3.2 HP Analysis

The HP analysis technique is only applicable when mesocyclonic rotation is present at cloud base, which means an HP value can only be computed for a small portion of the homogeneous simulations. In the boundary simulation, a persistent and organized low-level mesocyclone is present from 7200 s through the end of the simulation, thus an HP value can be computed at each time step after the development of the low-level mesocyclone. In the warm side simulation, low-level rotation is present from 1980 s until 2340 s; however the HP value is zero through this period. By the time precipitation begins falling near the mesocyclone, rotation has already dissipated at low levels. The modified warm side simulation is very similar to the warm side, but has a non-zero HP value at one time step; therefore it is included in the time series (Figure 3.10). Both of the cool side simulations contain rotation at the low-levels; the original cool side simulation on the right flank from 2130 - 2490 s, and the modified cool side simulation on the left flank from 2670 - 3570 s. Again, the HP value is zero for the original cool side simulation, since the low-level rotation has decreased in intensity by the time precipitation begins falling near the mesocyclone. However, the HP values for modified cool side simulation are non-zero throughout the lifetime of the low-level rotation and range from 24.5 to 72 (Figure 3.10). Since the boundary storm contains a low-level mesocyclone for a long period of time, the HP values change greatly with time and appear to exhibit a cyclic pattern, but are generally in the range of 0 to 40 (Figure 3.10).

It is difficult to give much credence to HP values in either the original warm side storm or the original cool side storm, since the low-level mesocyclone is only present in the first few time steps of the simulation, which is before precipitation has a chance to form in either the forward or rear flank downdrafts. Only one time step contains a non-zero HP value for the modified warm side simulation (Figure 3.10); therefore it is not compared to the boundary simulation. However, it is possible to compare the HP values produced in the modified cool side simulation and the boundary simulation. Since the HP value is essentially a percentage of the low-level mesocyclone that contains precipitation, it makes sense that an unstable, shorter-lived mesocyclone could have higher HP values than a longer-lived storm. In fact, copious amounts of precipitation in the mesocyclone may be responsible for the demise of low-level mesocyclonic rotation in the modified cool side simulation. Unlike the modified cool side simulation, the boundary simulation never exceeds an HP value of 40, or 40 percent of the mesocyclone containing convective precipitation (Figure 3.10). Throughout the boundary simulation, a pattern is created: precipitation begins to fall in the low-level mesocyclone and causes the HP value increase, then the mesocyclone moves farther outside the falling precipitation and the HP value drops back to zero. This pattern is not seen in the homogeneous storms, and appears to relate to the ability of the low-level updraft to transition outside areas of precipitation. In the following subsection, this behavior is examined further.

3.3 Storm Splitting Analysis

A major transition that occurs in the boundary storm is a split which begins approximately 30 minutes after precipitation forms at the surface. This split is driven by a local deepening of the cool airmass by outflow from precipitation (Figure 3.11), which creates forced ascent similar to a gust front. A new updraft forms near the surface (~50 m) at 3720 s and strengthens, with the split occurring at mid-levels around 4320 s, and this updraft becomes stronger than the original by 4800 s. In the time series of vertical vorticity (Figure 3.1), this period of time is characterized by lower overall maximum values in mesocyclone strength, before a sharp increase which begins at 4920 s. This pattern correlates well to the time series of maximum vertical velocity (Figure 3.2), where overall updraft strength increases strongly beginning at 4800 s.

After the formation of the new updraft, the boundary storm has more of an east-northeasterly storm motion, as was mentioned in the time series analysis, and remains the dominant updraft throughout the remainder of the simulation. This change in propagation is not the typical deviation which takes place when a storm becomes supercellular (Rotunno and Klemp 1982); the boundary storm contains a mesocyclone and a negative pressure perturbation within the mesocyclone before the split occurs. Instead, this change in storm motion is due to the development of the boundary storm's gust front. Before splitting, forced ascent along the storm's outflow is not strong enough to produce a low-level updraft (Figure 3.12). Once the

combination of the cool airmass and gust front is strong enough to produce a new updraft, splitting occurs, after which the air entering the main updraft is forced up along the gust front. This induces new storm motion and pulls the low-level updraft away from precipitation.

Splitting occurs and gust fronts are present in the homogeneous simulations (Figures 3.13 and 3.14); however, it is the strength of the combined gust front and cool airmass in the boundary simulation, which allows for continual transitioning of the updraft away from precipitation, that distinguishes the boundary storm from homogeneous storms. In homogeneous simulations, splitting occurs early and is driven by the shape of the hodograph (Bunkers et al. 2000) rather than by redevelopment along a gust front; in fact, the forced ascent along the gust fronts produced in homogeneous storms does not produce a low-level updraft that is strong enough to continually draw inflow from outside the region of precipitation. Time series analysis previously demonstrated that mesocyclones in the homogeneous simulations are quickly immersed in precipitation, which is similar to the early behavior of the storm produced in the boundary simulation. The updrafts in homogeneous storms are never able to transition outside precipitation, thus the storms are not able to persist. In contrast, the strength of the combined gust front and cool airmass in the boundary simulation allows for stronger forced ascent, and the boundary storm is therefore able to develop a new updraft outside the region of precipitation, to split, and then continue to ingest warm air.

The ability of the low-level updraft in the boundary storm to transition away from precipitation appears in the time series of maximum vertical vorticity (Figure

3.1) as a cyclic pattern in mesocyclone strength, and as a cyclic pattern in HP values (Figure 3.10). Although the mesocyclone is largely steady state after splitting occurs, weakening and re-strengthening of the mesocyclone can be observed throughout the remainder of the simulation, and this pattern can be related to transitions of the location of the low-level updraft relative to precipitation. As precipitation begins falling in the low-level updraft, the response is an overall decrease in vertical vorticity; however as precipitation in the low-level updraft increases, outflow pushes farther away from the low-level updraft and it begins to transition away from precipitation, allowing the mesocyclone to strengthen. This transitioning behavior of the low-level updraft and cyclic behavior of the vertical vorticity is an important difference between the boundary storm and the storms produced in homogeneous simulations, and is apparent across a wide spectrum of analyses.

3.4 Trajectory Analysis

From analysis in the previous sections, it is clear that the boundary storm exhibits characteristics that make it fundamentally different than the homogeneous storms. To examine the precise effect of the boundary on mesocyclone development, trajectories are calculated to examine the source of air parcels traveling into the mesocyclone and to determine how positive vertical vorticity in the mesocyclone is generated. Tracers are placed in the mid-level mesocyclone at multiple times and then are backwards integrated to determine their source region. The mid-level mesocyclone is considered to be where vertical vorticity exceeds 0.01 s^{-1} at 5 km, and tracers are placed in this vertical slice with a horizontal spacing of 200 m. Trajectory positions are calculated with a large time step of 120 s (history files are stored every 120 s during the simulation) and a small time step of 30 s, which requires interpolation of tracer positions between history files.

Early in the simulation (from 1920 s – 3840 s), all tracers which terminate in the mid-level mesocyclone originate on the warm side of the boundary, at multiple vertical levels (Figure 3.15). These tracers are pulled toward the mesocyclone by storm inflow and are then ingested by the updraft. As the storm moves further north over the cool side of the boundary, parcels terminating in the mid-level mesocyclone are drawn both from the warm airmass and from inside the cooler airmass, (Figure 3.16). Although some tracers originate on the warm side of the boundary, are lifted over the boundary, and then settle into the cooler airmass, the trajectories are split

into two groups for the purpose of analysis: those originating from inside the cool side airmass, and those originating and remaining in the warm side environment until ingestion in the mesocyclone. Although this eliminates a number of trajectories from analysis, it provides a better delineation between tracers that experience enhancement from the boundary and tracers that do not. From 3840 s through the end of the simulation, there are at least two trajectories in each category, and the number of trajectories which originate in the cool airmass increases with increasing time.

After dividing the trajectories into groups, tracers are evaluated in two ways: a time series of vertical vorticity, and a time series of the contributions to the vertical vorticity tendency (Equation 1.1). One representative tracer is selected from each group for each trajectory computation, in order to simplify the plots of the variables. For tracers that originate in both airmasses, initial values of vertical vorticity are zero, since no preexisting vertical vorticity is present in the domain. As the trajectories are ingested by the updraft, vertical vorticity increases dramatically for both trajectories originating in the warm side and for trajectories originating in the cool side (Figures 3.18 and 3.20). For tracers in the cool airmass, both stretching and tilting contribute positively to vertical vorticity tendency before the parcel is lifted into the mesocyclone, then the contribution from tilting becomes negative as the parcel is lifted above the boundary (Figures 3.17). In the warm airmass, tilting contributes positively to the vertical vorticity tendency, while stretching contributes negatively (Figures 3.19). The contribution from mixing, although plotted in Figures 3.17 and 3.19, is negligible for both warm and cool side trajectories. In both the

warm and cool sides of the boundary, initial vertical vorticity is generated via tilting of horizontal vorticity, after which vertical vorticity is available to be stretched and to contribute to the vertical vorticity in the mesocyclone. Therefore, the tendency of vertical vorticity in tracers from both sides of the boundary is primarily due to tilting of horizontal vorticity.

In order to evaluate how parcels from each airmass are contributing to the overall strength of the mesocyclone, the final value of vertical vorticity is analyzed for all trajectories that fall into one of the two groups. Interestingly, the largest values of vertical vorticity are from trajectories that originate and remain in the warm side until ingestion into the mesocyclone, while trajectories from the cool side of the boundary contribute only to the smallest values of vertical vorticity. This is consistent at all times for which trajectories were calculated, and can be seen in histograms that display the percentage of different vertical vorticity ranges contributed by each group of trajectories (Figure 3.21). Despite initially large amounts of horizontal vorticity available to be tilted into the mesocyclone, the cool side tracers are not resulting in large vertical vorticity. This is due to a negative contribution from tilting which occurs as the tracers are lifted by the updraft, beginning at approximately 2.5 km (Figure 3.22). Although horizontal shear at this level still contributes to positive tilting (Figure 3.23), it is a combination of both horizontal shear and horizontal gradients in vertical velocity that determine the sign of the tilting term (Equation 1.1). As trajectories enter the mesocyclone from the north, a negative contribution to vertical vorticity from tilting is produced by increasing values of vertical velocity as the tracer moves southward (Figure 3.24).

This results in a lower end value of vertical vorticity for trajectories originating in the cool side.

At low levels, trajectories terminating in the low-level (~1.5 km) mesocyclone originate almost exclusively from the cool side of the boundary (Figure 3.25). All trajectories, regardless of origination, travel through the cooler airmass before being ingested into the mesocyclone, and thus, all experience horizontal vorticity enhancement. Due to the combination of the cool airmass and the gust front created by the storm itself, all warm air is forced upward and does not enter the low-level updraft; thus the lack of contribution of tracers from the warm side to the vertical vorticity at cloud-base height. For trajectories entering the low-level mesocyclone, vertical vorticity is created primarily through stretching, which is reasonable in an area of forced ascent; however, tilting is also contributing to positive vertical vorticity when the tendency initially becomes positive (Figure 3.26 and 3.27). After boundary interaction, the cloud-base height updraft has a maximum speed of ~4 m s^{-1}; however, when the low-level mesocyclone forms, the vertical velocity at cloud-base height is ~9 m s^{-1}, which indicates a large enough contribution from stretching to obtain vertical vorticity exceeding 0.01 s^{-1} at low levels. As was discussed earlier, an increasing number of trajectories terminating in the mid-level mesocyclone originate in the cool side as the storm progresses, which implies that the low-level mesocyclone is supplementing rotation at mid-levels, and is helping to support the longevity of the supercell.

By the time the boundary storm becomes relatively steady state, it is well over the cool side airmass. Therefore, it could be expected that the homogeneous

cool side simulation would develop in a manner similar to the boundary storm. As was discovered in the time series analysis, this is clearly not the case; although the homogeneous cool side and modified cool side storms both contain mesocyclones for a period of time, neither are able to achieve the behavior of the persistent and steady-state mesocyclone found in the boundary storm. This is most likely due to the failure of the right-splitting component to develop into a supercell. Without augmentation of vertical velocity from an airmass boundary, the updraft on the right-splitting storm is very weak and dissipates quickly, as was discussed in previous sections. The left-moving storm is odd in that the mesocyclone is cyclonic and develops on the western side of the storm. Storm motion of the left-mover is to the NNW, which means precipitation is not propagating the in same direction as the gust front on the western flank of the storm; therefore it cannot maintain the strength seen in the boundary storm. Without the support of strong forced ascent from a combination of the gust front and cooler airmass, the updraft is not able to continually pull in air away from falling precipitation. As a result, the updraft becomes embedded in precipitation as the gust front weakens, and the storm is not able to persist.

Table 3.1. Start and end times of the mid-level mesocyclone in seconds for each simulation, and the lifetime of each mesocyclone in minutes.

	Start time (s)	**End time (s)**	**Lifetime (min)**
Warm	1980	3780	30
Modified Warm	2640	4260	27
Cool	2130	5010	48
Modified Cool	2130	6810	78
Boundary	1920	14400	208

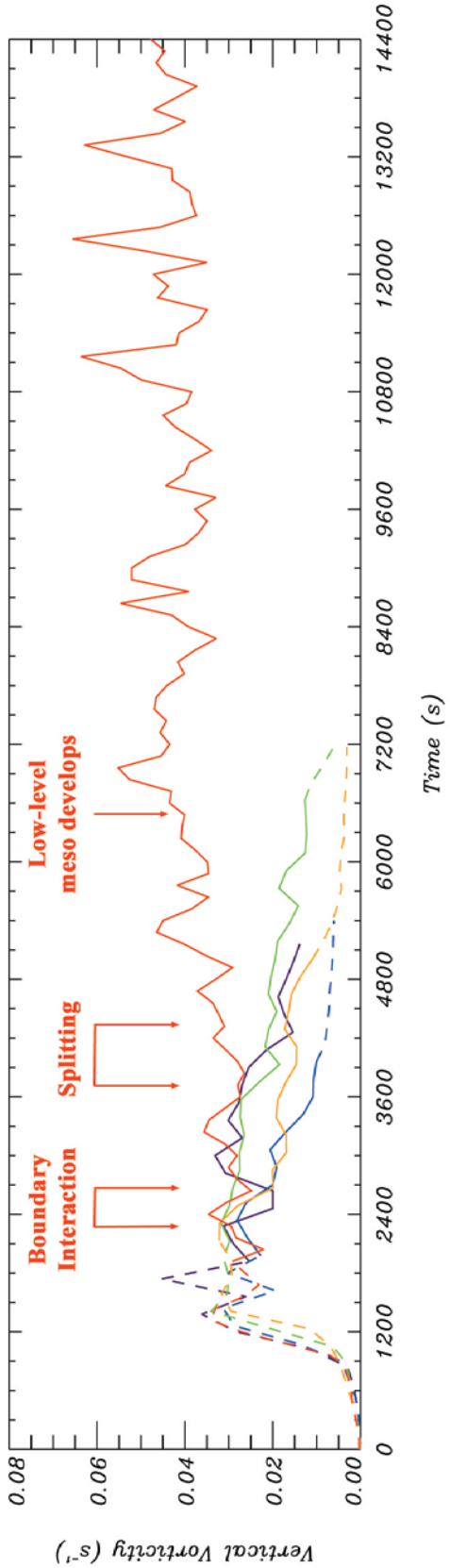

Figure 3.1. A time series of maximum vertical vorticity throughout the entire depth of the domain for the boundary simulation (red), modified cool side simulation (green), cool side simulation (orange), warm side simulation (blue), and modified warm side simulation (purple). Dashed lines indicate that the storm does not meet mesocyclone criteria, either because precipitation has not yet reached the surface or vertical vorticity has fallen below 0.01 s^{-1}. Annotations on the figure apply only to the boundary simulation.

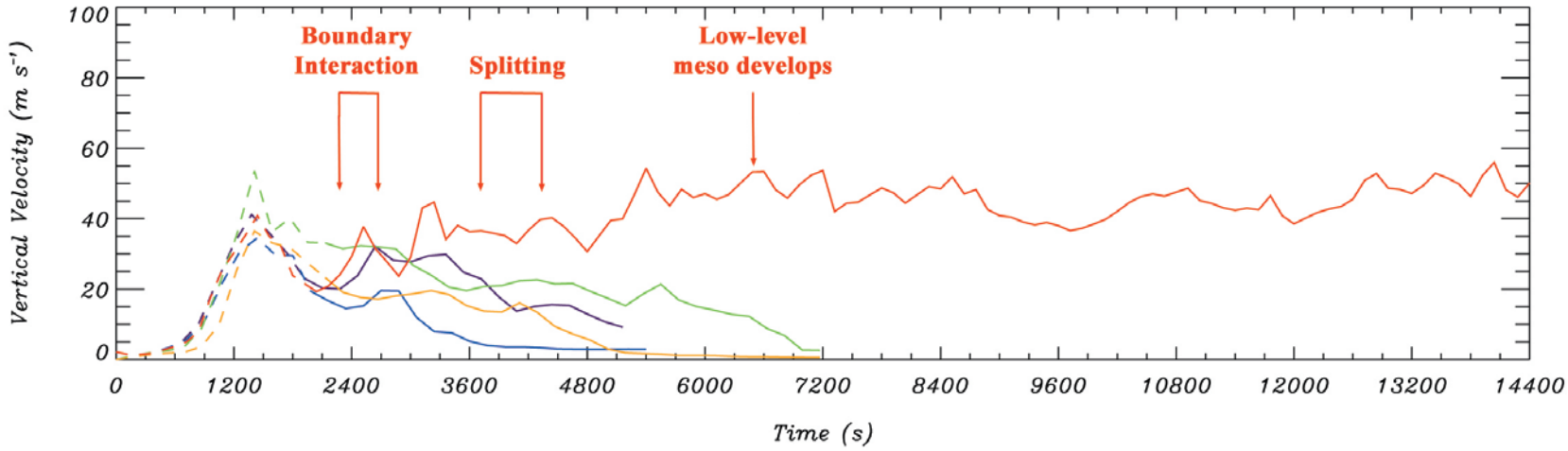

Figure 3.2. A time series of maximum vertical velocity throughout the entire depth of the domain for the boundary simulation (red), modified cool side simulation (green), cool side simulation (orange), warm side simulation (blue), and modified warm side simulation (purple). Dashed lines indicate that precipitation has not yet reached the surface. Annotations on the figure apply only to the boundary simulation.

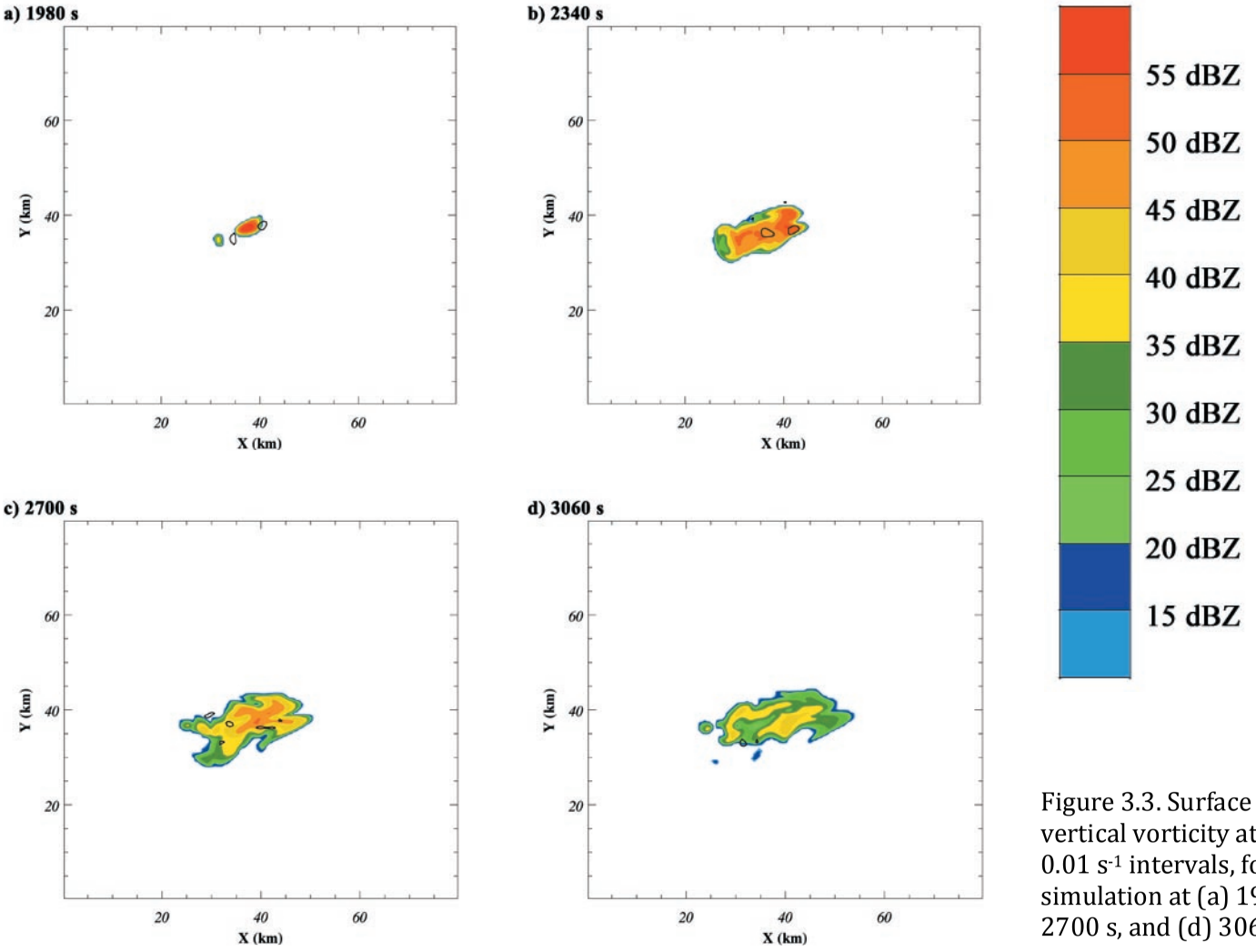

Figure 3.3. Surface reflectivity and vertical vorticity at 5 km, contoured at 0.01 s^{-1} intervals, for the warm side simulation at (a) 1980 s, (b) 2340 s, (c) 2700 s, and (d) 3060 s.

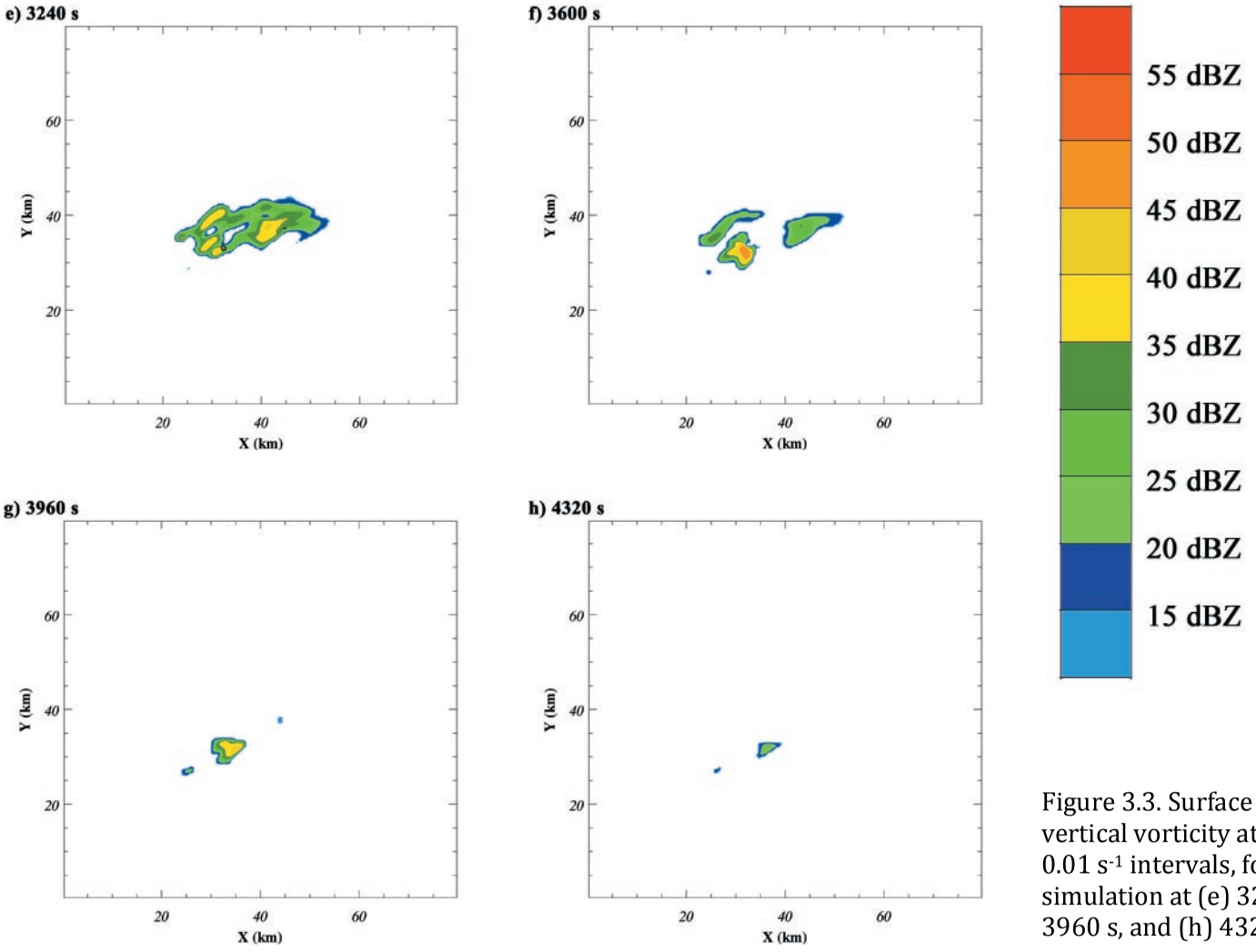

Figure 3.3. Surface reflectivity and vertical vorticity at 5 km, contoured at 0.01 s^{-1} intervals, for the warm side simulation at (e) 3240 s, (f) 3600 s, (g) 3960 s, and (h) 4320 s.

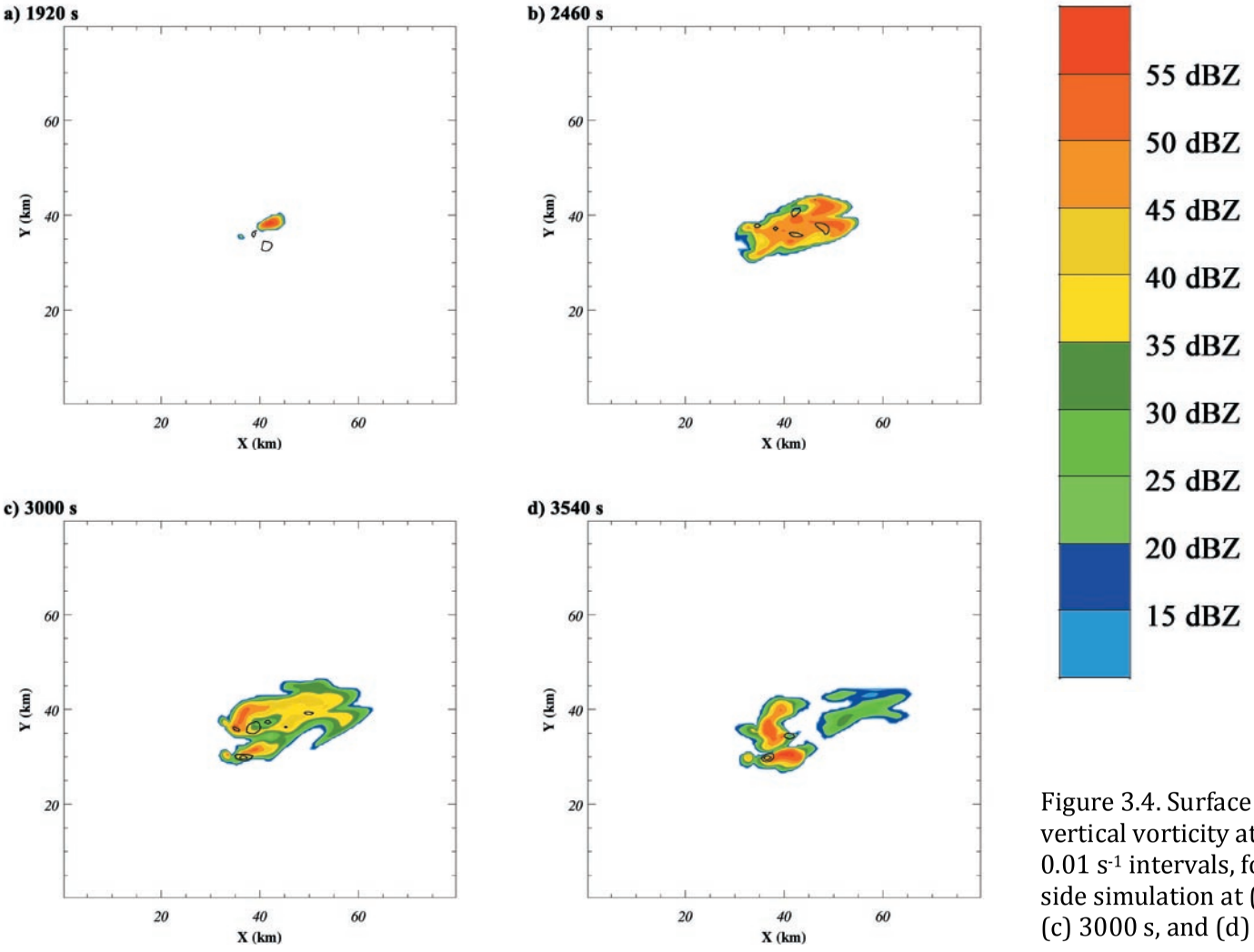

Figure 3.4. Surface reflectivity and vertical vorticity at 5 km, contoured at 0.01 s^{-1} intervals, for the modified warm side simulation at (a) 1920 s, (b) 2460 s, (c) 3000 s, and (d) 3540 s.

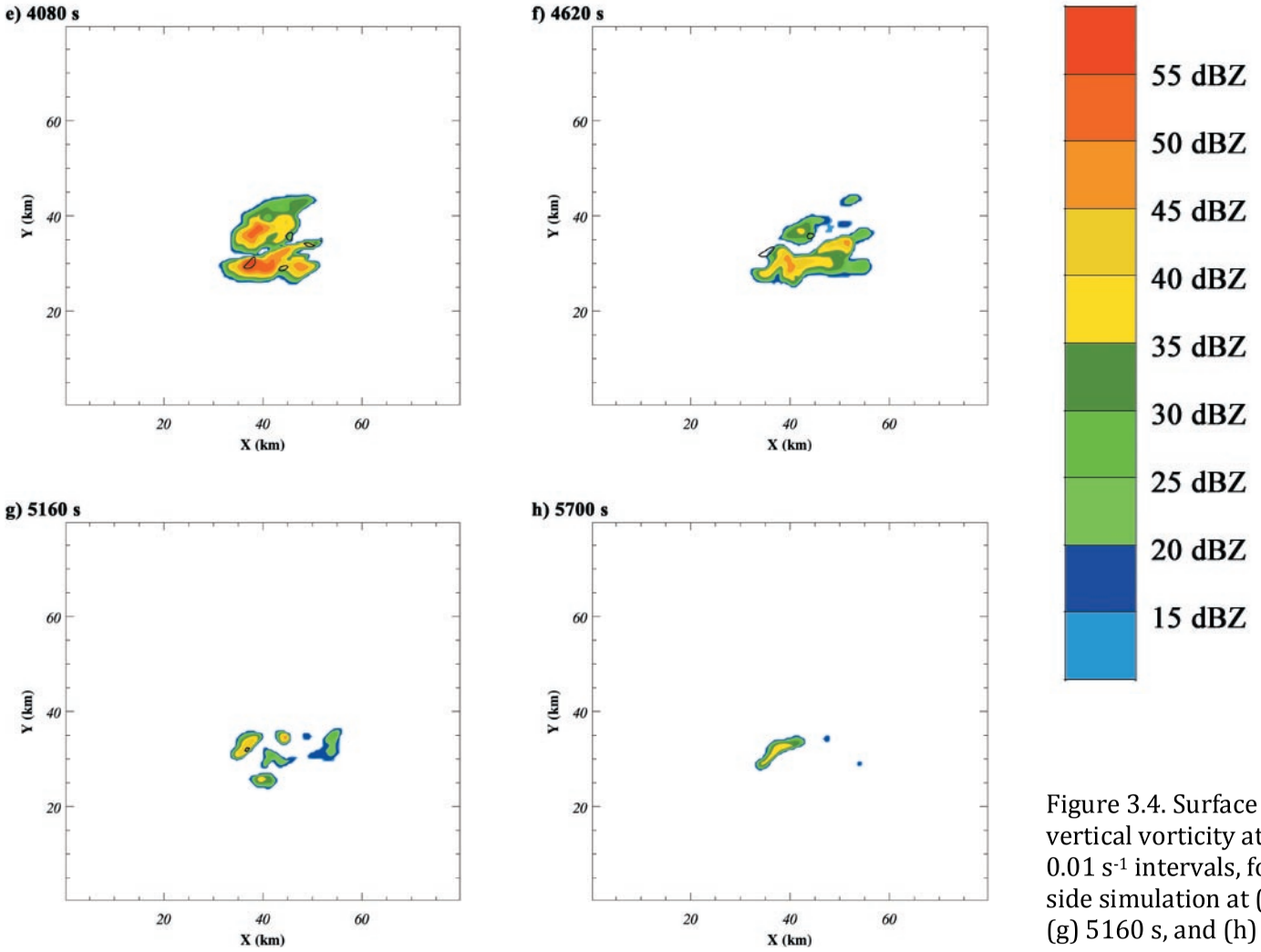

Figure 3.4. Surface reflectivity and vertical vorticity at 5 km, contoured at 0.01 s^{-1} intervals, for the modified warm side simulation at (e) 4080 s, (f) 4620 s, (g) 5160 s, and (h) 5700 s.

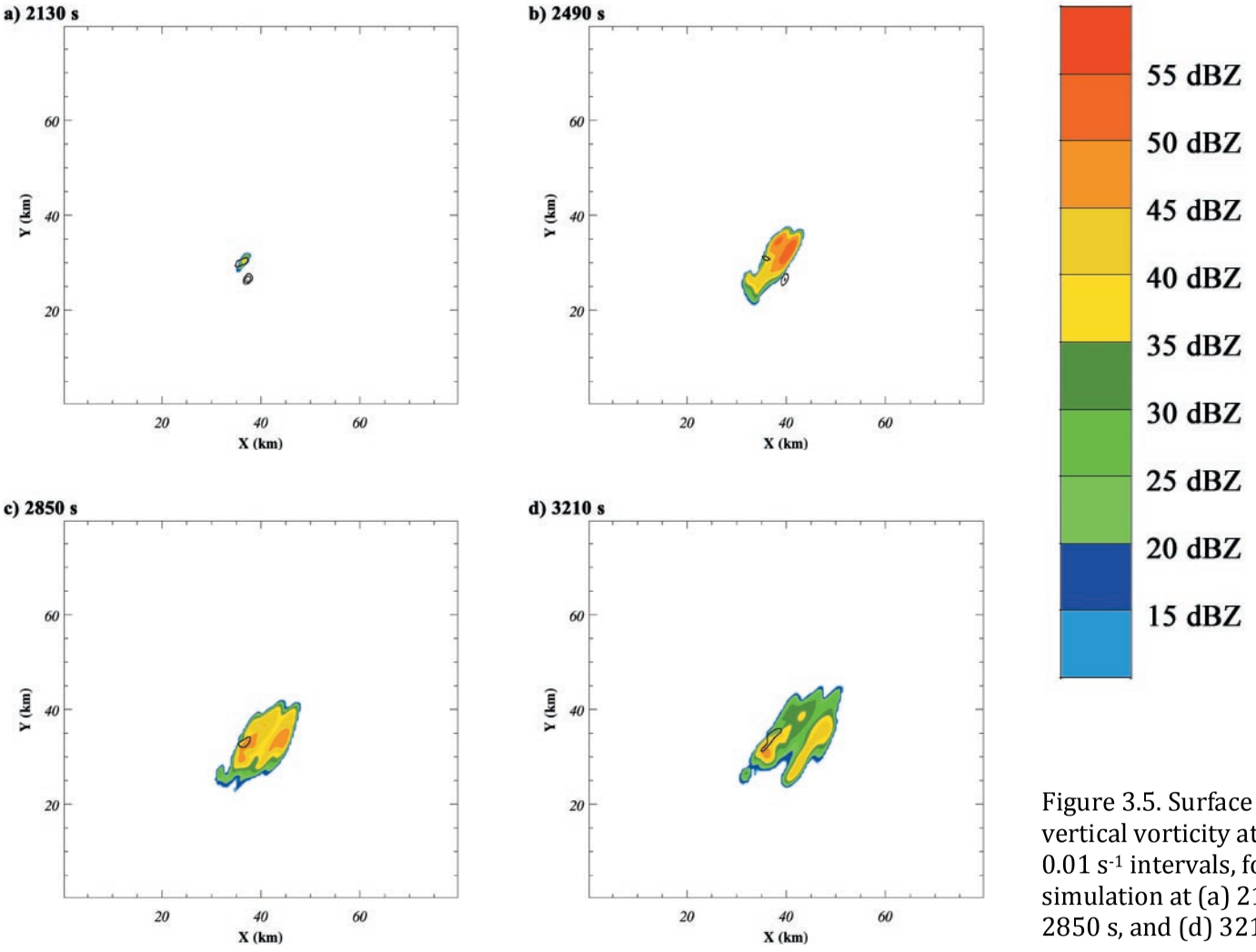

Figure 3.5. Surface reflectivity and vertical vorticity at 5 km, contoured at 0.01 s^{-1} intervals, for the cool side simulation at (a) 2130 s, (b) 2490 s, (c) 2850 s, and (d) 3210 s.

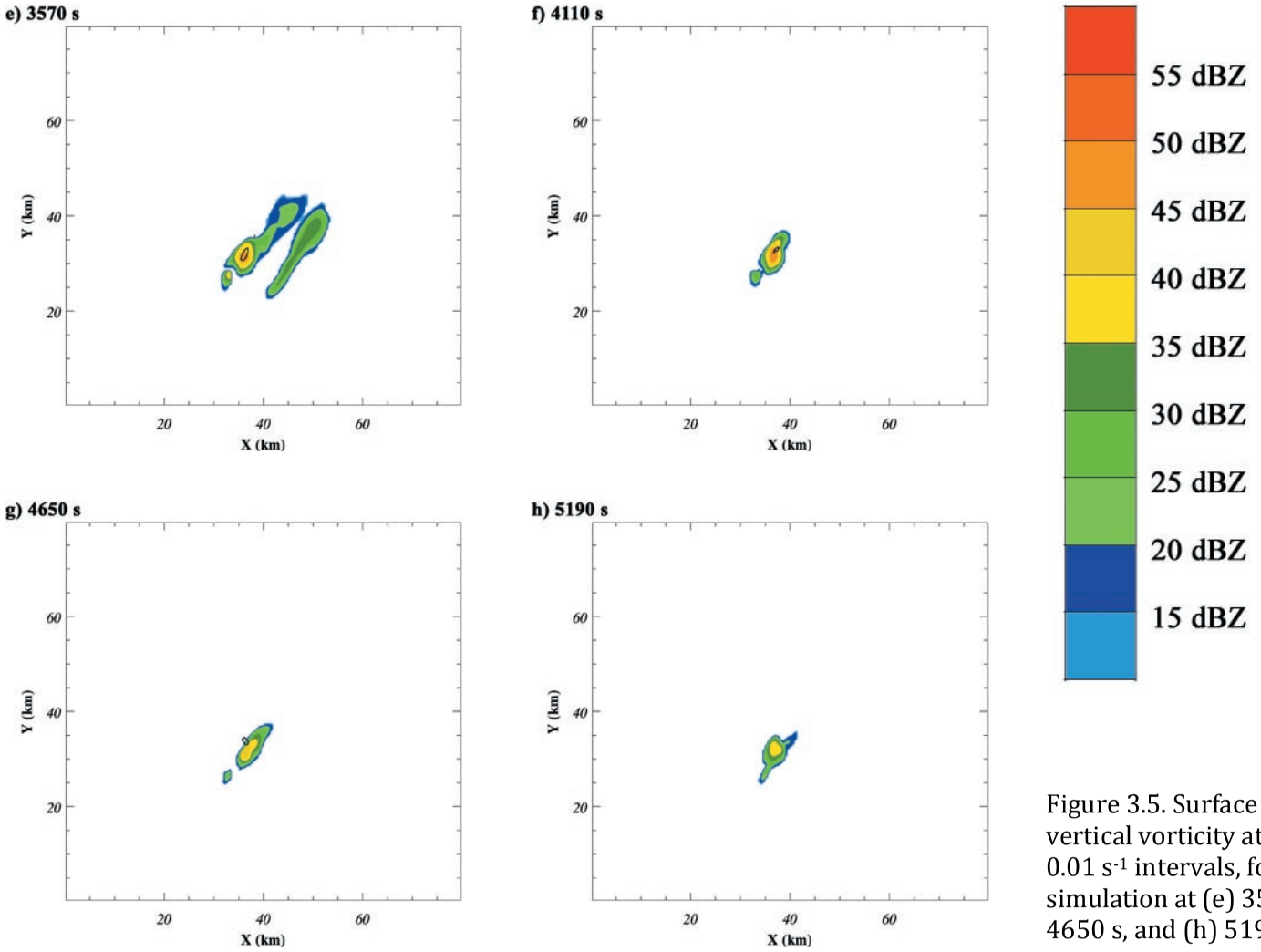

Figure 3.5. Surface reflectivity and vertical vorticity at 5 km, contoured at 0.01 s^{-1} intervals, for the cool side simulation at (e) 3570 s, (f) 4110 s, (g) 4650 s, and (h) 5190 s.

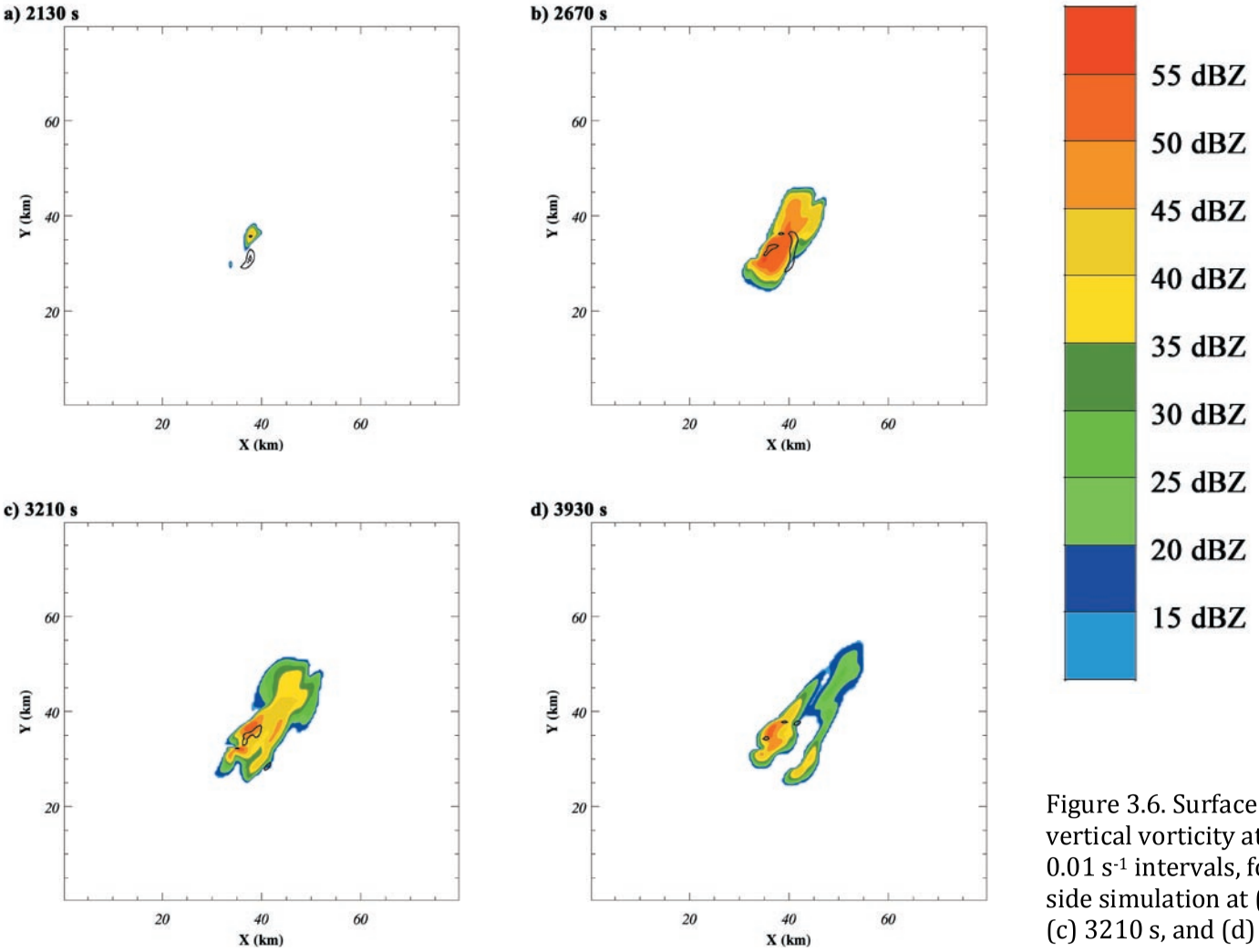

Figure 3.6. Surface reflectivity and vertical vorticity at 5 km, contoured at 0.01 s^{-1} intervals, for the modified cool side simulation at (a) 2130 s, (b) 2670 s, (c) 3210 s, and (d) 3930 s.

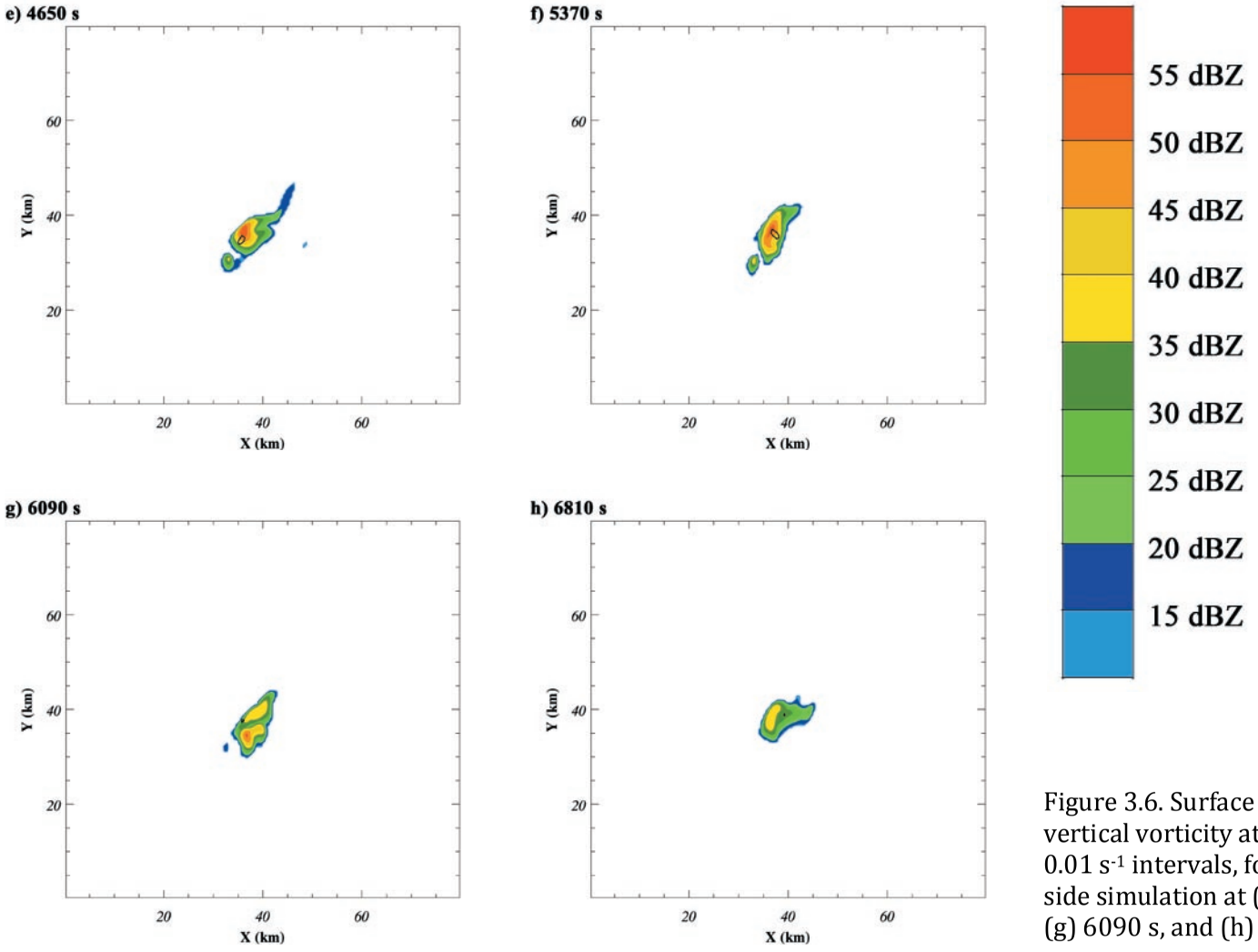

Figure 3.6. Surface reflectivity and vertical vorticity at 5 km, contoured at 0.01 s^{-1} intervals, for the modified cool side simulation at (e) 4650 s, (f) 5370 s, (g) 6090 s, and (h) 6810 s.

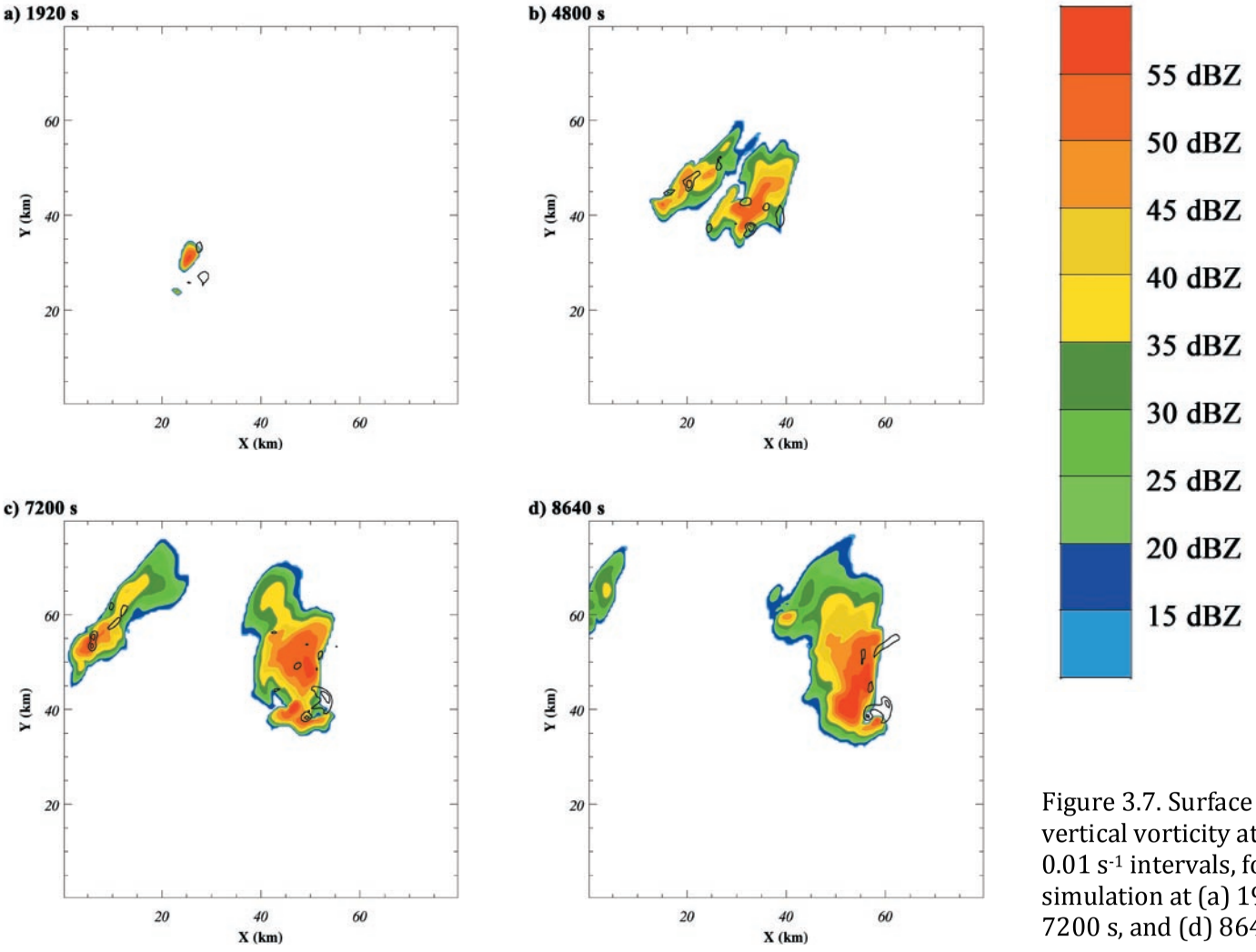

Figure 3.7. Surface reflectivity and vertical vorticity at 5 km, contoured at 0.01 s^{-1} intervals, for the boundary simulation at (a) 1920 s, (b) 4800 s, (c) 7200 s, and (d) 8640 s.

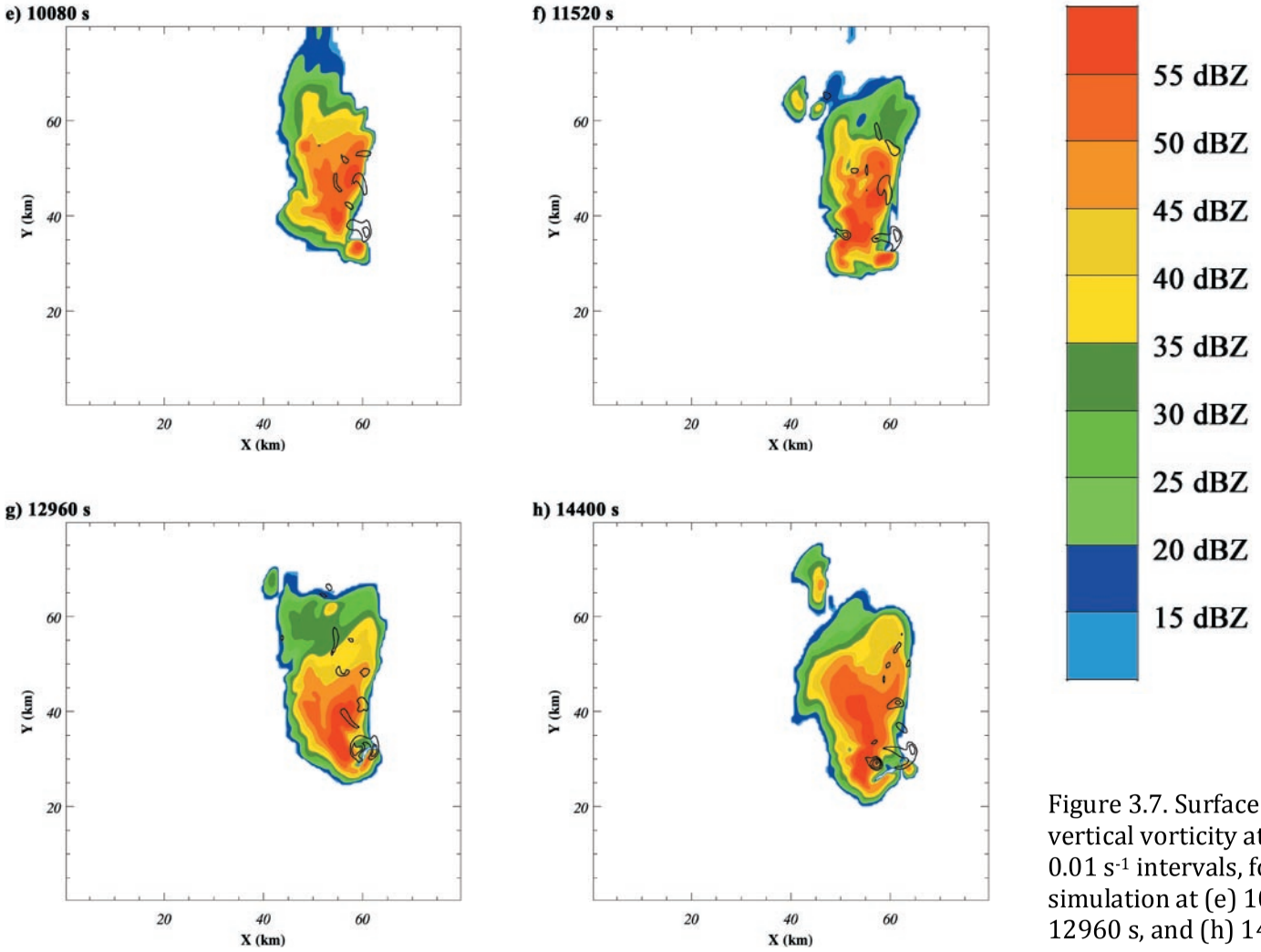

Figure 3.7. Surface reflectivity and vertical vorticity at 5 km, contoured at 0.01 s^{-1} intervals, for the boundary simulation at (e) 10080 s, (f) 11520 s, (g) 12960 s, and (h) 14400 s.

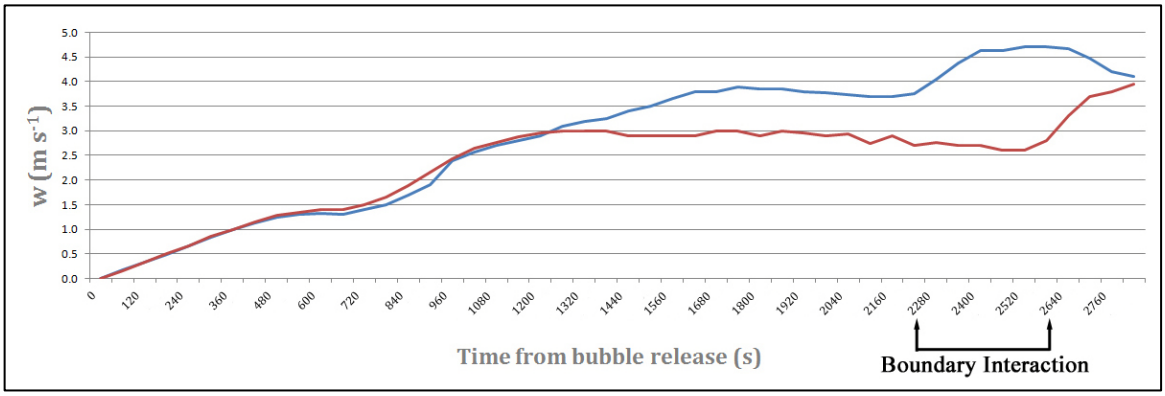

Figure 3.8. Time series of 0.5 km vertical velocity for the homogeneous warm side storm (red) and boundary storm (blue).

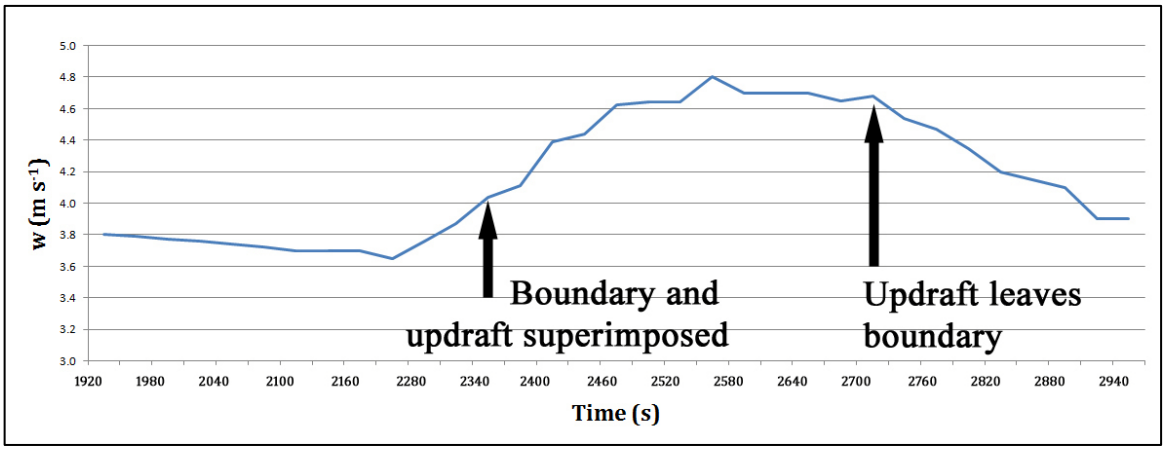

Figure 3.9. Time series of vertical velocity at 0.5 km for the boundary storm, during boundary interaction.

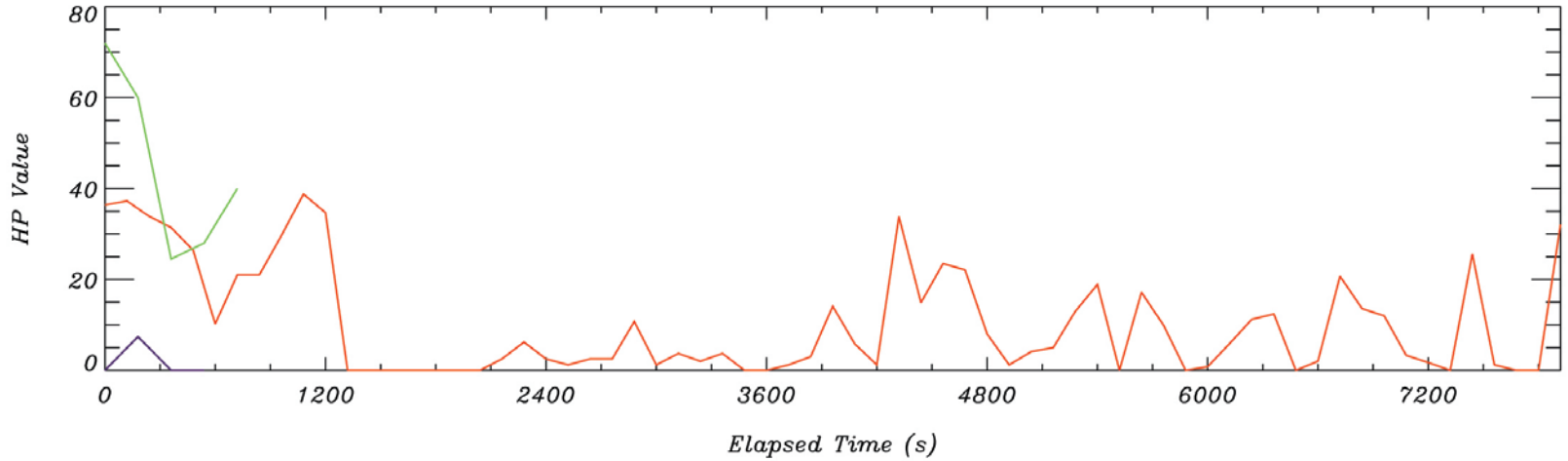

Figure 3.10. Time series of HP values for the boundary storm (red), modified cool side simulation (green), and modified warm side simulation (purple). Elapsed time = 0 s corresponds to the time that the low-level mesocyclone formed in each simulation.

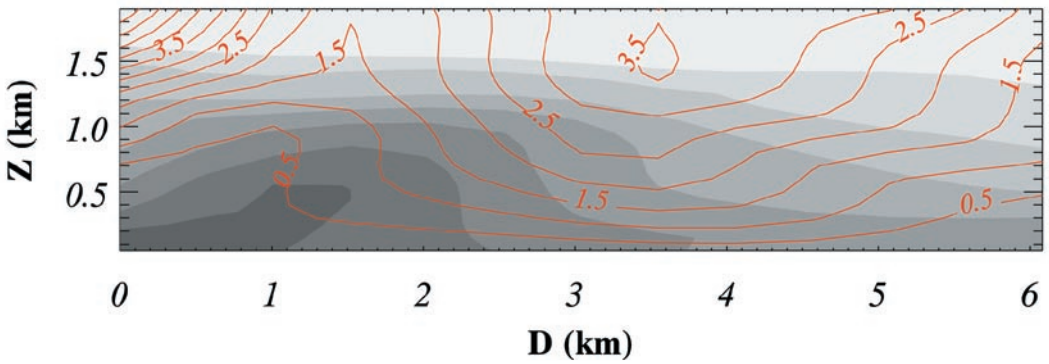

Figure 3.11. Cross section of virtual potential temperature (shaded at 1 K intervals) and vertical velocity (red contours at 0.5 m s^{-1} intervals) for the boundary simulation at 4200 s. The lightest gray represents a virtual potential temperature of 312 K, with values decreasing thereafter.

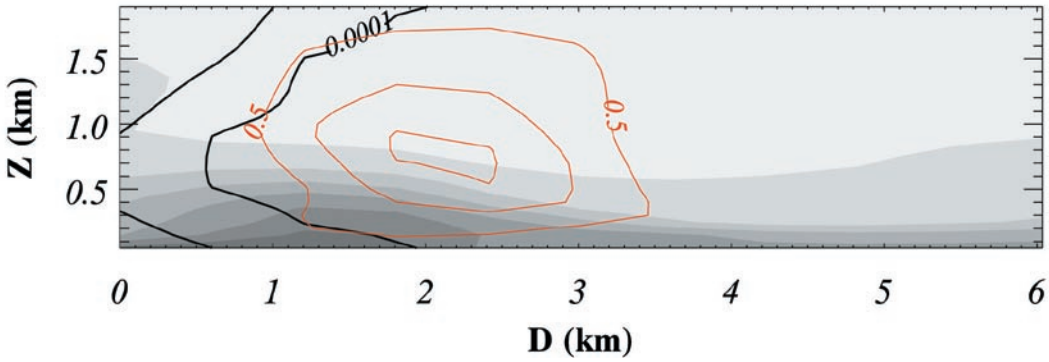

Figure 3.12. Cross section of virtual potential temperature (shaded at 1 K intervals), rain water and hail mixing ratios (black contours at 10^{-4} g kg^{-1} intervals), and vertical velocity (red contours at 0.5 m s^{-1} intervals), for the boundary simulation at 2400 s. The lightest gray represents a virtual potential temperature of 312 K, with values decreasing thereafter.

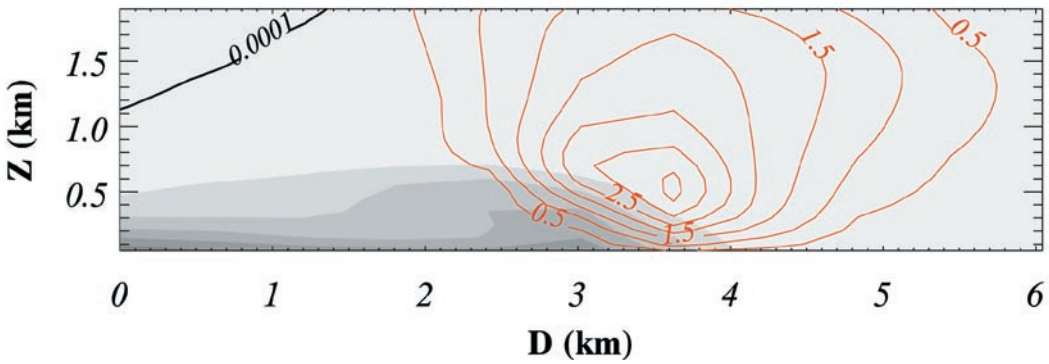

Figure 3.13. Cross section of virtual potential temperature (shaded at 1 K intervals), rain water and hail mixing ratios (black contours at 10^{-4} g kg^{-1} intervals), and vertical velocity (red contours at 0.5 m s^{-1} intervals), for the homogeneous warm side simulation at 2700 s. The lightest gray represents a virtual potential temperature of 312 K, with values decreasing thereafter.

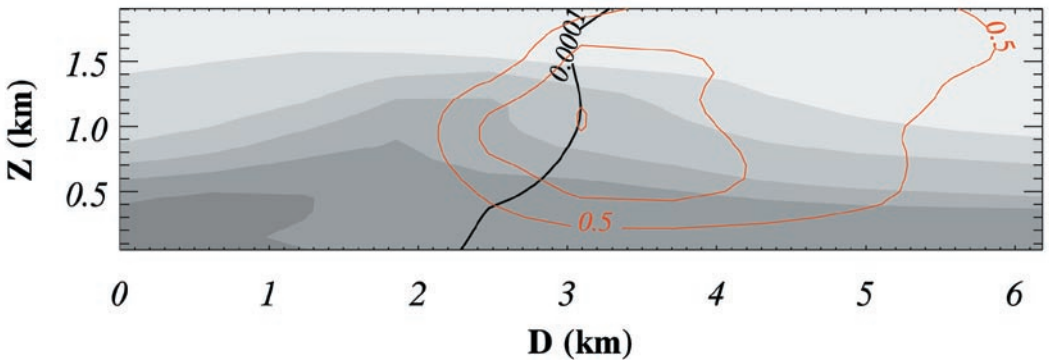

Figure 3.14. Cross section of virtual potential temperature (shaded at 1 K intervals), rain water and hail mixing ratios (black contours at 10^{-4} g kg^{-1} intervals), and vertical velocity (red contours at 0.5 m s^{-1} intervals), for the homogeneous cool side simulation at 3210 s. The lightest gray represents a virtual potential temperature of 312 K, with values decreasing thereafter.

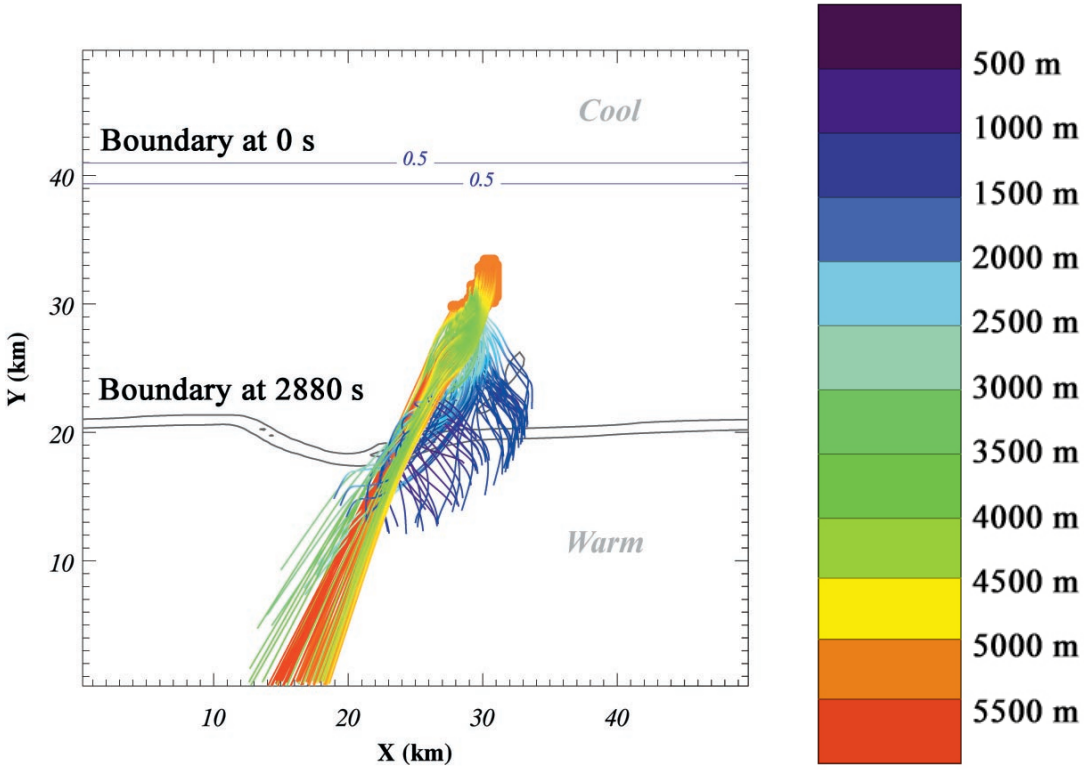

Figure 3.15. Boundary position at 0 s and 2880 s, and tracks of all trajectories terminating in the mid-level mesocyclone at 2880 s. Colors of the trajectories represent height in the domain, following the legend on the right.

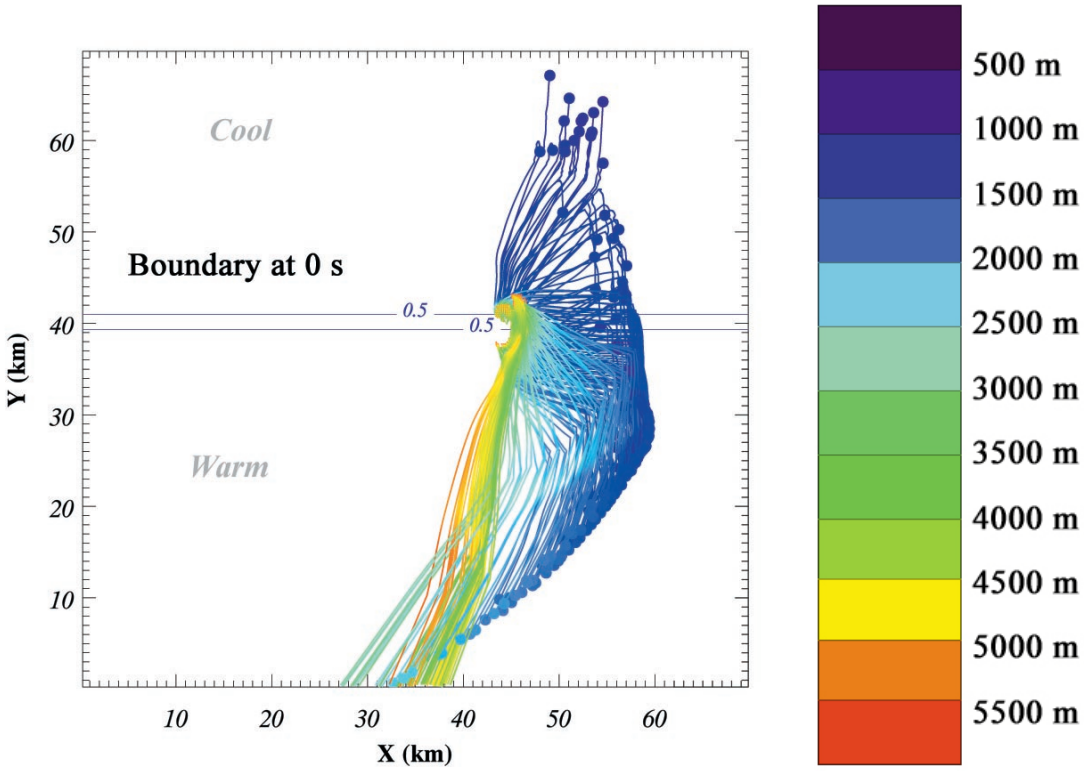

Figure 3.16. Boundary position at 0 s and tracks of all trajectories terminating in the mid-level mesocyclone at 6000 s. Colors of the trajectories represent height in the domain, following the legend on the right.

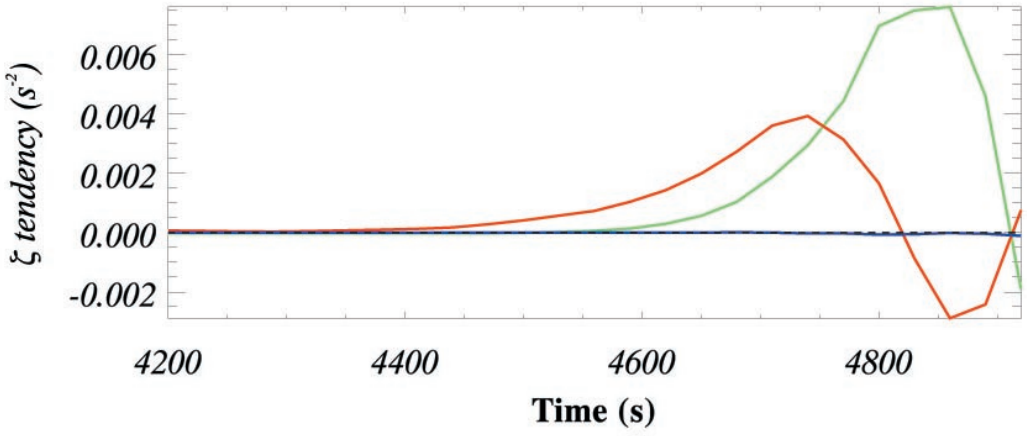

Figure 3.17. The contributions to vertical vorticity tendency from tilting (red), stretching (green) and mixing (blue) for a trajectory representing tracers originating in the cool side of the boundary, scaled by a value of 10^2.

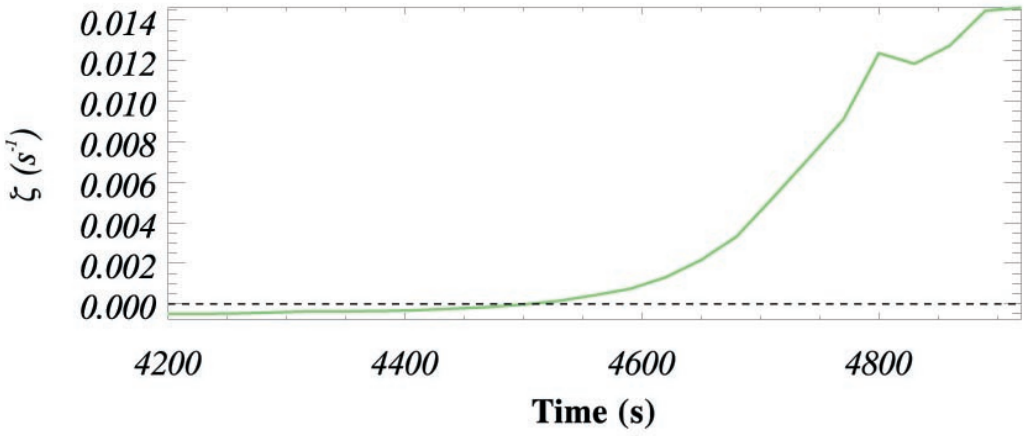

Figure 3.18. Vertical vorticity for a trajectory representing tracers originating in the cool side of the boundary.

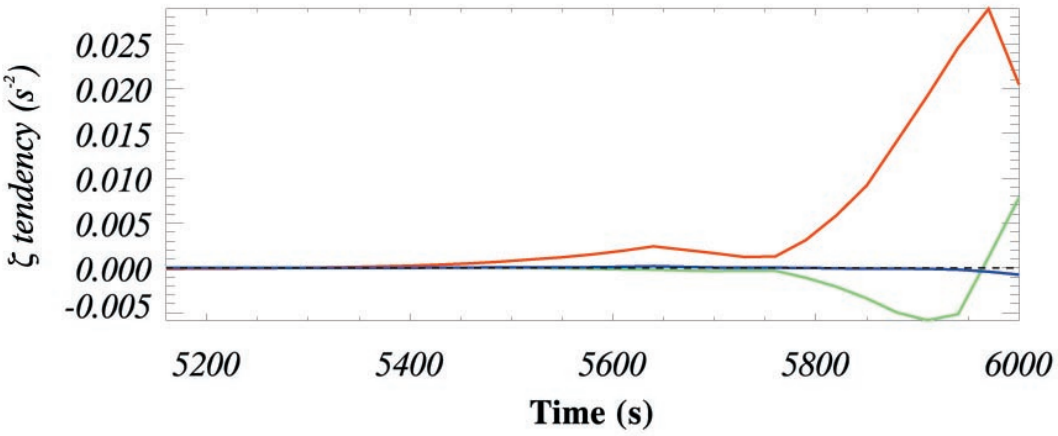

Figure 3.19. The contributions to vertical vorticity tendency from tilting (red), stretching (green) and mixing (blue) for a trajectory representing tracers originating in the warm side of the boundary, scaled by a value of 10^2.

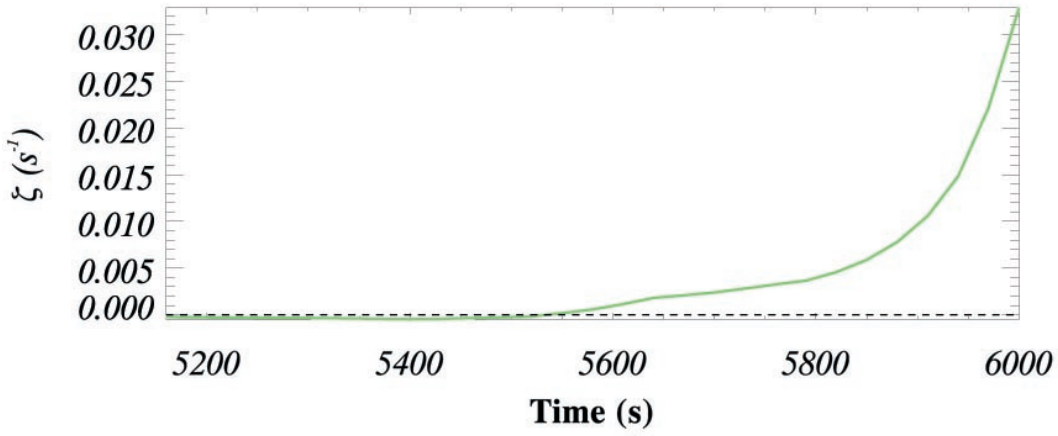

Figure 3.20. Vertical vorticity for a trajectory representing tracers originating in the warm side of the boundary.

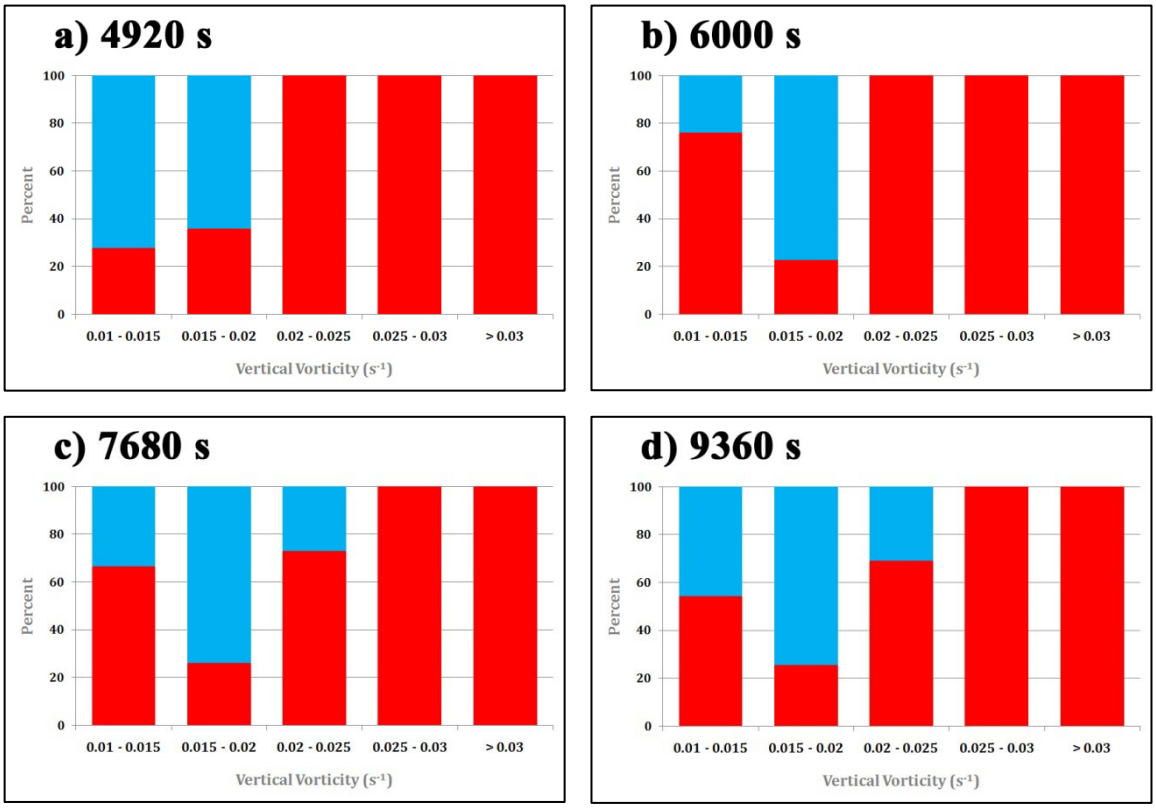

Figure 3.21. Histograms of the contribution from cool side trajectories (blue) and warm side trajectories (red) to vertical vorticity in the mid-level mesocyclone at (a) 4920 s, (b) 6000 s, (c) 7680 s, and (d) 9360 s.

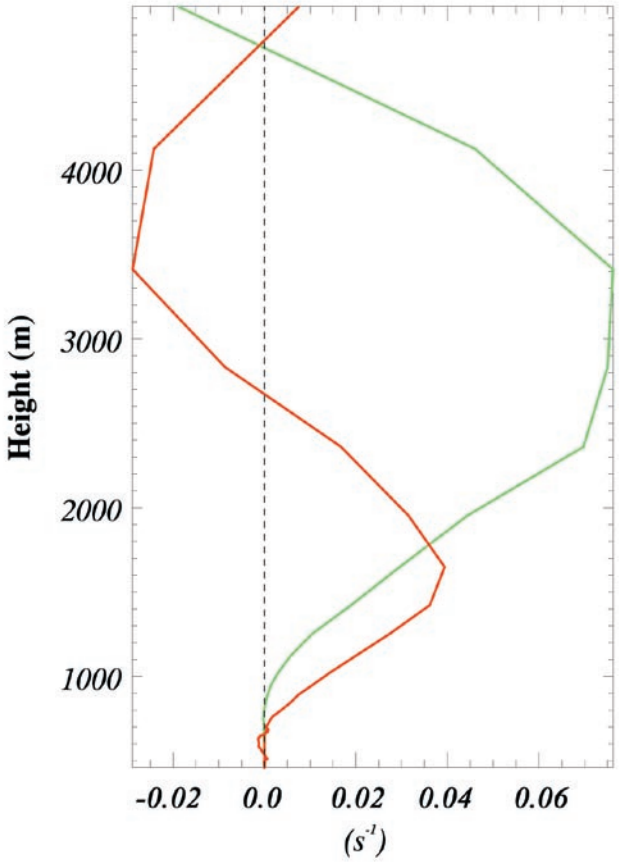

Figure 3.22. Vertical profile of the contributions to vertical vorticity from stretching (green) and tilting (red) for a trajectory representing tracers originating in the cool side of the boundary and terminating in the mid-level mesocyclone.

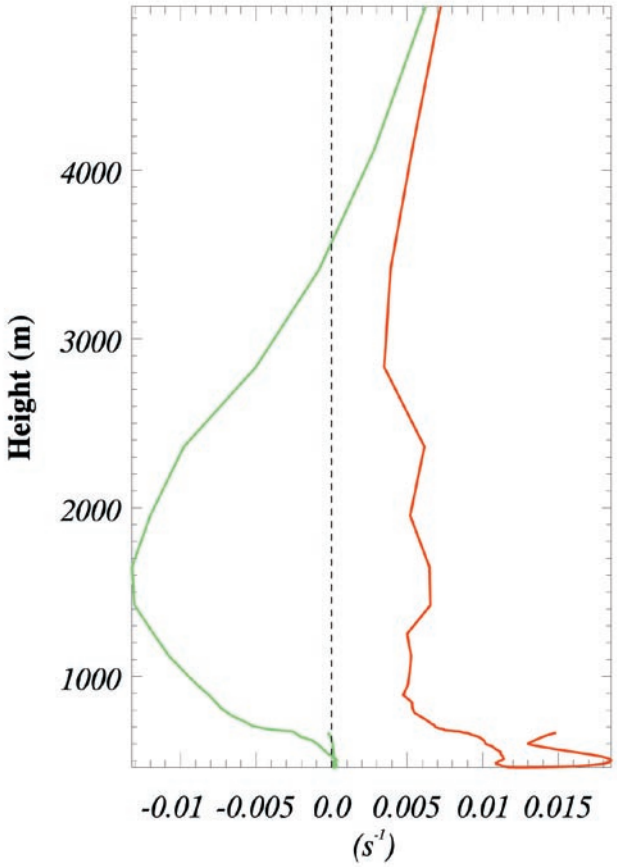

Figure 3.23. Vertical profile of vertical shear in the u-direction (green) and the y-direction (red) for a trajectory representing tracers originating in the cool side of the boundary and terminating in the mid-level mesocyclone.

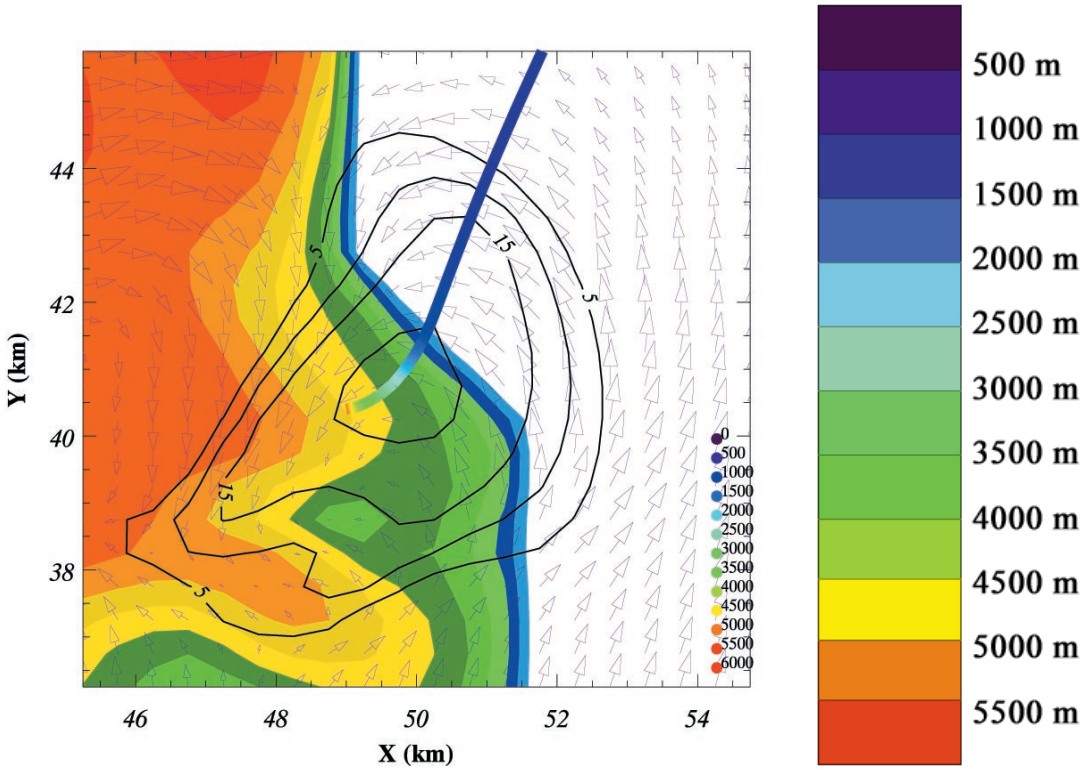

Figure 3.24. The path of a trajectory representing tracers originating in the cool side of the boundary and terminating in the mid-level mesocyclone at 6840 s. Shading is surface reflectivity, arrows are wind vectors at 3.5 km, and contouring is vertical velocity at 3.5 km, contoured at 5 m s^{-1} intervals. Colors of the trajectory represent height in the domain, following the legend on the right.

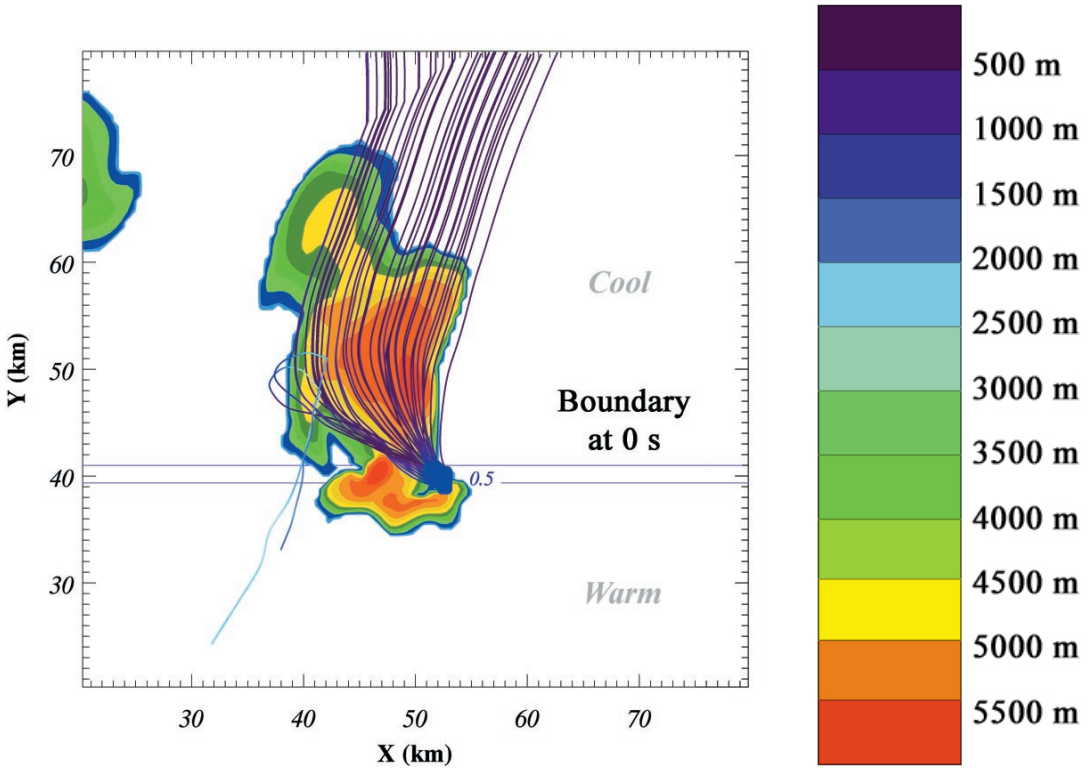

Figure 3.25. The position of the boundary at 0 s and the tracks of all trajectories terminating in the 1.5 km mesocyclone for the boundary simulation at 7200 s. Colors of the trajectories represent height in the domain, following the legend on the right.

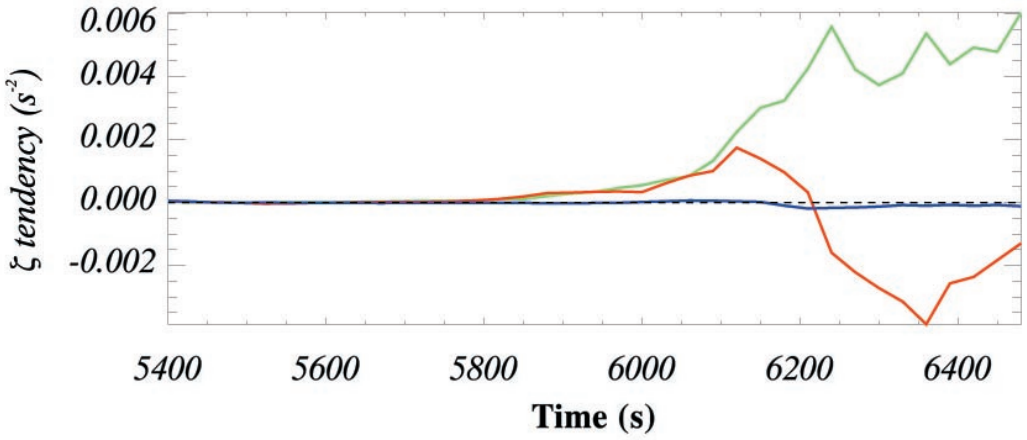

Figure 3.26. The contributions to vertical vorticity tendency from tilting (red), stretching (green) and mixing (blue) for a trajectory representing tracers terminating in the low-level mesocyclone, scaled by a value of 10^2.

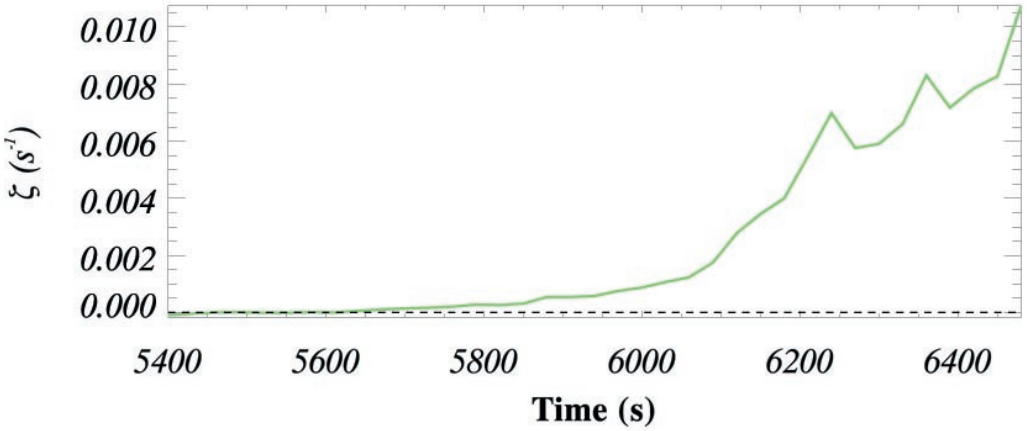

Figure 3.27. Vertical vorticity for a trajectory representing tracers terminating in the low-level mesocyclone.

Chapter 4

Conclusions and Summary

Overall, the boundary storm is stronger, longer-lived, and much more classical (Figure 4.1) in appearance than the other storms which are produced. All storms generated in homogeneous environments have maximum vertical vorticity of ~0.03 s^{-1}, while the boundary storm reaches a value that is more than double this amount after the mesocyclone becomes more steady-state. The boundary storm is also much longer-lived than any of the homogeneous-environment storms. It is clear that the boundary simulation produces a much more prototypical supercell than any of the homogeneous simulations, despite having the same CAPE and environmental shear as the original warm side simulation. The presence of the boundary impacts the supercell in three ways: 1) by enhancing the updraft and allowing a stronger right-splitting storm to develop, 2) by combining with storm outflow to produce forced ascent which allows the storm to transition away from precipitation and continually draw in warm air, and 3) by providing enhanced horizontal vorticity that is ingested into the low-level updraft and supports the development and maintenance of a low-level mesocyclone.

It is important to note that the storm produced in the boundary simulation propagates away from the airmass boundary, but still experiences a comparative

enhancement of mesocyclone strength and updraft strength throughout its life cycle. This implies that the boundary has an impact on the storm beyond the time that the storm is crossing the boundary and directly experiencing forced ascent. In fact, two of the previously discussed impacts of the boundary on the storm relate to the presence of the cooler airmass and not the boundary itself; however, the boundary simulation differs from all of the homogeneous simulations, including the homogeneous cool side and modified cool side simulations. It is the combination of both direct storm interaction with the boundary and the presence of the cooler airmass that produces a typically structured and long-lived supercell.

From the results of this study, it can be concluded that the presence of a preexisting airmass boundary has a dominant effect on the strength and longevity of the storm produced in the boundary simulation. Forced ascent from the airmass boundary creates a stronger right-splitting storm that is able to persist long enough for a gust front to form and for splitting to occur. Once the storm has propagated over the cool airmass, the gust front and cool airmass combine to create forced ascent that promotes a long-lived supercell by allowing continual ingestion of warm air. In addition, enhanced horizontal vorticity from within the cooler airmass is continually ingested into the low-level updraft, which supports the presence and longevity of a low-level mesocyclone. Trajectories originating in the cool side are found at multiple levels in the mesocyclone, which provides support to a common assumption that the tilting of horizontal vorticity found in the denser side of an airmass boundary is important in supercell development (Markowski et al. 1998, Atkins et al. 1999, Rasmussen et al. 2000, etc.). In addition, the presence of the low-

level mesocyclone appears to be entirely a result of the horizontal vorticity enhancement found in the cool airmass, which is consistent with the results of Atkins et al. (1999). Although the results of this study are specific to one case, the common observance of supercell thunderstorms along airmass boundaries helps to support the application of these results to multiple cases and environments.

In operational meteorology, emphasis is placed on storms which develop along and interact with airmass boundaries. This study supports these findings and also places emphasis on the lasting effects of an airmass boundary on mesocyclone longevity and strength, and continues to support an operational emphasis on the recognition of airmass boundaries and their potential to impact a warning situation. In addition, this study opens the door for further research into the role of an airmass boundary on mid-level mesocyclogenesis, particularly in non-supercellular environments. Future work could include modeling additional cases in which a supercell forms along an airmass boundary in a classically non-supercellular environment, in order to judge the sensitivity of the mid-level mesocyclone to the warm side environment. Sensitivity tests of different vertical shear values or temperature perturbations in the airmass boundary could also be performed to judge the response of the mid-level mesocyclone. In addition, a follow-up study could expand on the role of forced ascent along the boundary to both low-level and mid-level mesocyclone strength. In summary, this study not only provides new insight into the role of horizontal vorticity in supercell development, but also encourages further study into the topics discussed herein.

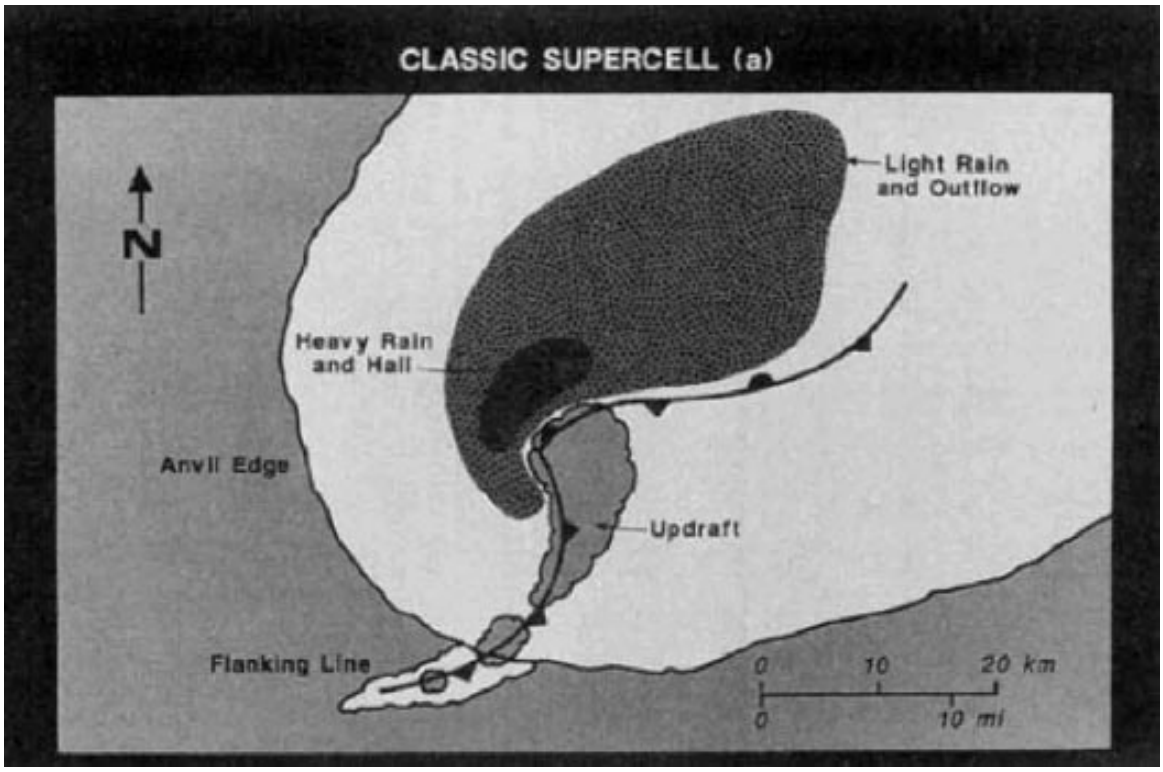

Figure 4.1. Schematic of a classic supercell, from Moller et al. (1994).

Acknowledgements

We thank the University of Nebraska-Lincoln Department of Geosciences and a University of Nebraska Layman Award for providing the funding to support this work, as well as the Research Computing Facility (RCF) at the University of Nebraska-Lincoln for technical support and resources.

References

Atkins, N. T., M. L. Weisman, and L. J. Wicker, 1999: The influence of preexisting boundaries on supercell evolution. *Mon. Wea. Rev.,* **127**, 2910-2927.

Beatty, K. A., J. M. Straka, E. N. Rasmussen, and L. R. Lemon, 2004: A quasi-objective method for discrimination of supercell archetypes using the WSR-88D. Preprints, *22nd Conf. on Severe Local Storms*, Hyannis, MA, Amer. Meteor. Soc.

Browning, K. A., 1964: Airflow and precipitation trajectories within severe local storms which travel to the right of the winds. *J. Atmos. Sci*., **21**, 634-639.

Bunkers, M. J., B. A. Klimowski, J. W. Zeitler, R. L. Thompson, and M. L. Weisman, 2000: Predicting supercell motion using a new hodograph technique. *Wea. Forecasting*, **15**, 61-79.

Davies, J. M., 1993: Wind and instability parameters associated with supercell and non-supercell tornado events in the southern high plains. Preprints, *17th Conf. on Severe Local Storms*, St. Louis, MO, Amer. Meteor. Soc., 51-55.

Davies-Jones, 1984: Streamwise vorticity: The origin of updraft rotation in supercell storms. *J. Atmos. Sci*, **41**, 2991-3006.

Davies-Jones, R. P., R. J. Trapp, and H. B. Bluestein, 2001: Tornadoes and tornadic storms. *Severe Convective Storms, Meteor. Monogr*., No. 50, Amer. Meteor. Soc., 167-221.

Dostalek, J. F., J. F. Weaver, and G. L. Phillips, 2004: Aspects of a left-moving tornadic thunderstorm of 25 May 1999. *Wea. Forecasting*, **19**, 614-626.

Doswell, C. A., III, 2001: Severe convective storms - an overview. *Severe Convective Storms, Meteor. Monogr.*, C. A. Doswell III, Ed., No. 28, Amer. Meteor. Soc., 1-26.

Fierro, A. O., M. S. Gilmore, E. R. Mansell, L. J. Wicker, and J. M Straka, 2006: Electrification and lightning in an idealized boundary-crossing supercell simulation of 2 June 1995. *Mon. Wea. Rev.*, **134**, 3149-3172.

Geerts, B., R. Damiani, and S. Haimov, 2006: Finescale vertical structure of a cold front as revealed by an airborne doppler radar. *Mon. Wea. Rev.*, **134**, 251-271.

Gilmore, M. S., J. M. Straka, and E. N. Rasmussen, 2004: Precipitation evolution sensitivity in simulated deep convective storms: Comparisons between liquid-only and simple ice and liquid phase microphysics. *Mon. Wea. Rev.*, **132**, 1897-1916.

Hart, J. A., and W. Korotky, 1991: The SHARP workstation v1.50 users guide. National Weather Service, NOAA, U.S. Department of Commerce, 30 pp.

Houston, A. L., 2004: The role of preexisting airmass boundaries in the maintenance and rotation of deep convection in a high-CAPE, low-shear environment. Ph.D. thesis, Department of Atmospheric Sciences, University of Illinois at Urbana-Champaign, 275 pp.

Houston, A. L., and D. Niyogi, 2007: The sensitivity of convective initiation to the lapse rate of the active cloud-bearing layer. *Mon. Wea. Rev.,* **135**, 3013-3032.

Houston, A. L., R. L. Thompson, and R. Edwards, 2008: The optimal bulk wind differential depth and the utility of the upper-tropospheric storm-relative flow for forecasting supercells. *Wea. Forecasting*, **23**, 825-837.

Klemp, J. B., and R. Wilhelmson, 1978: The simulation of three-dimensional convective storm dynamics. *J. Atmos. Sci*, **35**, 1070-1096.

Maddox, R. A., L. R. Hoxit, and C. F. Chappell, 1980: A study of tornadic thunderstorm interactions with thermal boundaries. *Mon. Wea. Rev.*, **108**, 322-336.

Markowski, P. M., E. N. Rasmussen, and J. M. Straka, 1998: The occurrence of tornadoes in supercells interacting with boundaries during VORTEX-95. *Wea. Forecasting*, **13**, 852-859.

Mesinger, F., G. DiMego, E. Kalnay, K. Mitchell, P. C. Shafran, W. Ebisuzaki, D. Jović, J. Woollen, E. Rogers, E. H. Berbery, M. B. Ek, Y. Fan, R. Grumbine, W. Higgins, H. Li, Y. Lin, G. Manikin, D. Parrish, and W. Shi, 2006: North American Regional Reanalysis. *Bull. Amer. Meteor. Soc.*, **87**, 343–360.

Moller, A. R., C. A. Doswell, III, M. P. Foster, and G. R. Woodall, 1994: The operational recognition of supercell thunderstorm environments and storm structures. *Wea. Forecasting*, **9**, 327-347.

Rasmussen, E. N., and D. O. Blanchard, 1998: A baseline climatology of sounding-derived supercell and tornado forecast parameters. *Wea. Forecasting*, **13**, 1148-1164.

Rasmussen, E. N., S. Richardson, J. M. Straka, P. M. Markowski, and D. O. Blanchard, 2000: The association of significant tornadoes with a baroclinic boundary on 2 June 1995. *Mon. Wea. Rev.*, **128**, 174-191.

Rotunno, R. and J. B. Klemp, 1982: The influence of the shear-induced pressure gradient on thunderstorm motion. *Mon. Wea. Rev.*, **110**, 136-151.

Smith, P. L. J., C. G. Myers, and H. D. Orville, 1975: Radar reflectivity factor calculations in numerical cloud models using bulk parameterization of precipitation. *J. Appl. Meteor.*, **14**, 1156-1165.

Thompson, R. L., R. Edwards, J. A. Hart, K. L. Elmore, and P. M. Markowski, 2003: Close proximity soundings within supercell environments obtained from the Rapid Update Cycle. *Wea. Forecasting*, **18**, 1243-1961.

Weisman, M. L., and J. B. Klemp, 1982: The dependence of numerically simulated convective storms on vertical wind shear and buoyancy. *Mon. Wea. Rev*., **110**, 504-520.

Wicker, L. J., and R. B. Wilhelmson, 1995: Simulation and analysis of tornado development and decay within a three-dimensional supercell thunderstorm. *J. Atmos. Sci.*, **52**, 2675-2703.

Ziegler, C. L., and E. N. Rasmussen, 1998: The initiation of moist convection at the dryline: Forecasting issues from a case study perspective. *Wea. Forecasting*, **13**, 1106-1131.